J. Fluid Mech. (1992), *vol.* 240, *pp.* 133–166
Printed in Great Britain

Interaction of electrostatic and fluid dynamic fields in wire–plate electrostatic precipitators

By G. A. KALLIO† AND D. E. STOCK
Department of Mechanical and Materials Engineering, Washington State University, Pullman, WA 99164, USA

(Received 26 February 1990 and in revised form 2 December 1991)

Gas flow through wire–plate electrostatic precipitators is influenced by a secondary flow of electrical origin known as *electric wind*. This phenomenon arises when significant momentum is transferred from corona-generated ions to the gas. Electric wind can produce turbulence and recirculation. This complex flow field was characterized in a simple, three-wire precipitator by flow visualization, electrostatic and fluid dynamic numerical modelling, and laser-Doppler anemometry (LDA).

Velocity of seeded smoke was measured by two-component LDA. Coulomb effects were regionally eliminated by performing measurements along symmetry axes where the electric field and streamwise velocity component were mutually perpendicular. Coulomb drift velocities were also estimated from field charging theory to allow interpretation of measured transverse velocities. For a low inlet velocity (0.5 m/s), mean flow recirculation was evident and turbulence intensities as high as 50% were measured. Higher inlet velocities (1.0, 2.0 m/s) yielded no flow recirculation and lower turbulence levels that were polarity-dependent. Measured profiles of streamwise velocity showed that flow acceleration zones occurred upstream of each wire and also between wires near the collecting plate. The induced turbulence displayed significant inhomogeneity and anisotropy.

A combined finite-element, finite-difference electrostatic model was developed to yield ion density and electric field distributions within the precipitator. These predictions were used to incorporate an electric body force into a two-dimensional, turbulent fluid dynamic model based upon the k–ϵ formulation. The model predicted recirculating mean flow and turbulent diffusivities that were consistent with the smoke flow visualizations and LDA measurements.

1. Introduction

The use of electrostatic forces to separate fine particles (e.g. dust, fumes, and smoke) from the air has been known and employed for many decades. The process, known as electrostatic precipitation, was first applied commercially in 1906 by Frederick G. Cottrell, who built a device for separating sulphuric acid mist from its carrier gas (Cottrell 1914). Since that time, electrostatic precipitators (ESPs) have been developed into relatively efficient devices and play a major role in modern industrial particulate control. The basic process of electrostatic precipitation is straightforward: electric charge is placed on airborne particles which are driven toward collecting plates under the influence of an applied electrostatic field, i.e.

† Present Address: Department of Mechanical Engineering, California State University, Chico, CA 95929–0930, USA.

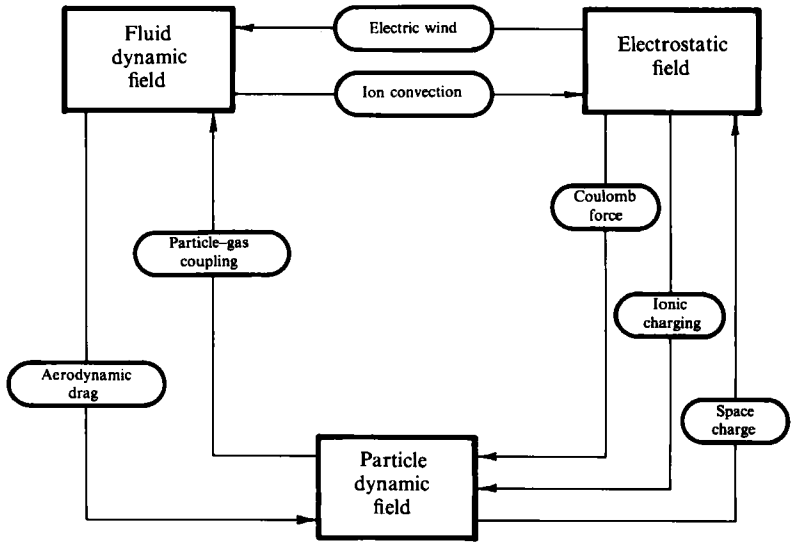

FIGURE 1. Interactive phenomena inside electrostatic precipitators.

Coulomb attraction. The particles acquire charge by exposure to a source of unipolar ions that attach to each particle. A corona discharge serves as the ion source, produced by the local electrical breakdown of gas in the vicinity of a sharp electrode (e.g. a fine wire or needle point) raised to a high d.c. voltage. The particles adhere to the collecting surface to form a continuous layer which can be effectively removed as large agglomerates by mechanical rapping or sonic agitation of the plate.

Despite a general understanding of ESP operation and its successful use in industry, many questions regarding particle collection remain unanswered. Moreover, theoretical formulations based upon unipolar particle charging and Coulomb transport in simple flow fields have not been reliable in predicting ESP performance. This is not surprising since there exists a very complex network of mechanisms that affect particle transport inside a precipitator. These phenomena are probably best understood as an interactive coupling of fluid dynamics, electrostatics, and particle dynamics. This conceptualization is shown in figure 1.

The existence of momentum coupling between the electrostatic (ionic) field and fluid dynamic field gives rise to a feature known as the *electric wind* (also termed the *ionic wind* or *corona wind*). This secondary gas flow results from corona-generated ions that collide at high velocity with neutral gas molecules residing in the space between the discharge electrode and collecting plate. The effect of the electric wind on the gas flow field and the resulting impact on particle transport is possibly the least understood of all the phenomena that occur within an ESP. It is known that the momentum imparted to the gas by the ion flux produces a highly directional gas flow (jet) toward the plate in the absence of flow through the precipitator. Continuity demands that gas return to the corona region, thereby promoting a recirculating flow. Inlet flow to the precipitator interacts with the electric wind to produce a highly complex fluid dynamic field.

The emphasis on coal-based power generation and advanced particulate control during the 1970s produced numerous detailed studies on the fundamental operation of ESPs. Included in these have been several efforts to better understand the electric wind and turbulent gas flow field. Ramadan & Soo (1969) numerically solved the

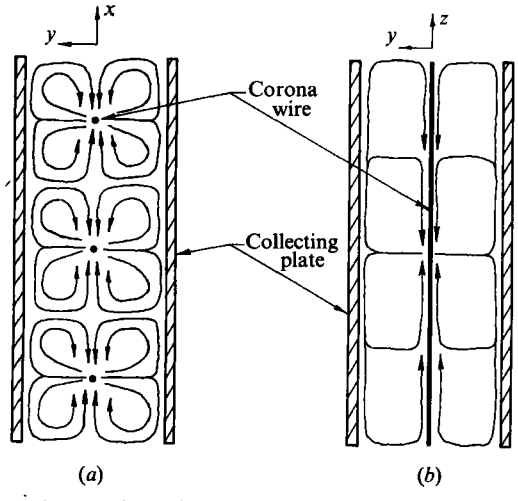

FIGURE 2. Reported secondary flows in wire–plate electrostatic precipitators due to the electric wind: (*a*) (x, y)-plane; (*b*) (y, z)-plane.

laminar, two-dimensional Navier–Stokes equations with electric body force for a constant space charge distribution to yield estimates of the electric-wind flow pattern in the (x, y)-plane (see figure 2*a*). Their model predicted that this secondary flow exists as a narrow, jet-like wind issuing from the corona wire toward the collecting plate in the absence of any inlet flow. The return flow was shown to be a diffuse, lower-velocity flow on either side of the corona wire. Similar results were found by Yabe, Mori & Hijikata (1978), who predicted the existence of two, identical, counter-rotating vortices in a single-wire, single-plate configuration.

Stock & Crowe (1974) numerically predicted the gas flow in a wire–pipe precipitator, including the effects of particle–gas and ion–gas (electric wind) momentum coupling. Owing to the symmetry of their geometry, the resulting velocity profile was unaffected by the electric wind. They concluded that electric-wind effects only arise when there exists asymmetry about the corona wire as in wire–plate precipitators. This conclusion was later substantiated by Flippen (1982), who examined the electric vorticity production term (rotational current density, $\nabla \times \boldsymbol{J}$) in the classical fluid vorticity equation for various geometries. His analysis proved that electrical vorticity is absent in geometries where the corona discharge is symmetric and uniform, but very significant in wire–plate configurations. He contended that electrical vorticity is solely responsible for the induced secondary flows.

The interaction of the electric wind with a superimposed inlet velocity was first theoretically investigated by Yamamoto & Velkoff (1981), who used a two-dimensional, streamline–vorticity numerical model. They demonstrated that inlet flow suppresses the electric wind-induced secondary flow in wire–plate precipitators. In addition, the incoming flow was found to gradually accelerate and be deflected toward the duct centreline owing to the formation of circulatory cells near the collecting plate. They applied their laminar model to both one-wire and two-wire configurations, finding that the existence of the electric wind was apparent for inlet velocities less than 1.2 m/s at typical corona current densities. The presence of a single circulatory cell opposite each wire became evident at a velocity of about 0.6 m/s. A pair of circulatory cells, as reported by others, was predicted for velocities

less than approximately 0.2 m/s. Their numerical results were qualitatively consistent with Schlieren flow visualization.

The turbulent aspects of precipitator gas flows were analysed by Bernstein & Crowe (1981), who applied a first-order, two-equation (k–ϵ) closure model to the time-averaged momentum equations. In their two-dimensional model, turbulence production was attributed solely to gradients in mean velocity, neglecting possible production or dissipation due to fluctuating electrical parameters. In addition to the electric wind, their analysis also included the effect of plate stiffeners, or baffles, on the gas flow and electric field. The electric field solution was approximated with a constant space charge density and the effect of the space charge on the applied electric field was neglected. Velocity vector maps of the mean flow in the (x, y)-plane were plotted, showing gas recirculation opposite the discharge wires due to electric wind, and downstream of the baffles due to flow separation. Electric-wind circulatory cells were predicted for inlet gas velocities as high as 1.7 m/s, but at excessively high electric fields (e.g. 80 kV across 0.1 m wire–plate spacing). The effect of electric-wind-generated turbulence on the mean flow was not presented, nor any turbulence quantities such as kinetic energy or eddy diffusivity.

Several detailed experimental investigations of electric wind have been undertaken using a variety of measurement methods. Robinson (1975) estimated velocities and eddy diffusivities from measured helium-tracer gas concentration profiles inside a full-width, positive corona, wire–plate ESP. His results indicated a recirculating gas flow pattern superimposed upon the streamwise flow. Interestingly, these secondary flows were detected in the (y, z)-plane of the precipitator (see figure 2*b* with no mention of recirculating flows in the (x, y)-plane as predicted and observed by others. Robinson hypothesized that these strong vertical flow components caused by the electric wind near the plate might contribute to re-entrainment of precipitated material and subsequent degradation in overall ESP performance. The streamwise (x-component) velocity profile was found to flatten under the influence of the corona discharge, thus raising the velocity gradient at the walls and contradicting the numerical results of Yamamoto & Velkoff. This flattened profile was attributed to the transverse electric wind transferring gas from mid-duct to the wall region.

Laser-Doppler anemometry (LDA) has provided experimentalists with a non-intrusive velocity measurement tool for evaluating the complex flow inside electrostatic precipitators. Gas velocities have been estimated by using small seed particles and assuming Coulomb drift to be negligible. This latter assumption is often tenuous and has been applied in several studies without complete justification.

Masuda *et al.* (1979) used LDA with 1.6 μm mean diameter particles to estimate the average and fluctuating components of gas velocity in a negative corona, wire–plate ESP. Their study detected average particle migration velocities nearly twice as high as those estimated from Coulomb attraction. The additional transverse velocity was attributed to the electric wind. The mean streamwise velocity increased near the collecting plate and decreased in the wire region, corroborating the findings of Robinson, but not those of Yamamoto & Velkoff. Recirculating secondary flows were not detected. However, significant turbulent effects were measured. The negative corona increased transverse r.m.s. velocity fluctuations but tended to suppress fluctuations in the streamwise direction. Power spectra analysis reveal increased high-frequency fluctuations for both directional components.

Leonard, Mitchner & Self (1983) employed LDA, hot-wire anemometry, Schlieren photography, and smoke-wise visualization to detect secondary flows and associated turbulence levels inside a bench-scale, wire–plate ESP. LDA measurements with

4 μm droplets in a positive corona device revealed streamwise velocity profiles that became more parabolic with increasing corona current densities. These results were in agreement with Yamamoto & Velkoff, but contradicted the findings of Robinson and Masuda *et al.*. This increase in core velocity was attributed to the formation of recirculating flows, which tended to squeeze the primary flow toward the centre of the duct. Flow loops in the vertical plane were not detected, but flow visualization indicated the existence of endwall vorticity in this plane. These vortices were attributed to corona quenching from electrical charging of the Plexiglas walls. Hot-wire anemometry was also employed to measure turbulence intensity at the precipitator exit. These results showed that negative corona markedly increased the total turbulent energy for inlet velocities less than about 2 m/s, but appeared to simply smooth the turbulence profile for higher velocities. Positive corona had little effect on turbulence energy production for inlet velocities greater than 2 m/s, but its presence inexplicably decreased the turbulence level at lower velocities. Smoke-wire visualization generally supported these measurements. The differing effects of positive and negative corona were attributed to the irregular, tuft-like structure of the negative discharge in contrast to the uniformity of the positive discharge. Kumaran (1983) performed hot-wire anemometry measurements similar to those of Leonard *et al.* (1983) at the exit of a full-width ESP. He found significant corona-induced turbulence for inlet velocities as high as 3 m/s at typical current densities. In contrast to Leonard *et al.*, he observed both production and redistribution of turbulence with positive corona. These differences were attributed to the different ESP aspect (height/width) ratios used in the two studies.

Thomsen *et al.* (1982) used LDA with 2–5 μm glycerin droplets to determine velocity vector maps and turbulence levels inside a full-width, negative corona wire–plate precipitator. Using a variety of discharge electrode shapes, they found the flow to be strongly three-dimensional for inlet velocities less than 1 m/s and moderate current densities. Their flow displayed distinct recirculation patterns in both the (x, y)- and (y, z)-planes. A smooth-wire electrode produced measured turbulence intensities in the range of 5–10%, based upon the average inlet velocity. A barbed-wire electrode generated a five-fold increase in corona current and corresponding turbulence levels as high as 40%. The Coulomb drift contribution to the measured mean and fluctuating velocities was not addressed.

Davidson (1984) investigated turbulence generation in a large-scale laboratory precipitator operating under negative corona. Velocity measurements using hot-film anemometry were performed at the exit of a 20:1 aspect ratio precipitator. Her results displayed a three-fold increase in turbulence intensity at an inlet velocity of 1 m/s and a six-fold increase at 0.5 m/s for moderate currents. A saturation effect was observed in the measured turbulence intensity as a function of current density, attributed to a more uniform corona discharge pattern at higher current values. No significant effect on the mean flow was detected. Turbulence power spectra displayed additional energy at all frequencies due to electric wind, with most energy corresponding to large-scale (low-frequency) motions.

The turbulence produced by the electric wind is thought to be at least comparable to other sources of precipitator gas flow turbulence such as wall shear, plate stiffener recirculation, and inlet flow expansion. All these sources contribute to particle dispersion, the importance of which was first recognized by Deutsch (1922). He reasoned that dispersion was dominant to the extent that a nearly uniform particle concentration profile could be assumed in the plane normal to the inlet flow. The well-known Deutsch efficiency theory has been widely used for several decades, even

though it typically overpredicts industrial ESP performance. Empirical corrections to the Deutsch theory have been incorporated to account for non-Deutschian phenomena such as re-entrainment, gas sneakage, and finite particle mixing. Such modifications obviously compromise the applicability of the model. More recent studies have attempted to improve the Deutsch theory by solving the time-averaged particle mass conservation equation by use of a gradient-diffusion (Boussinesq) approximation (Williams & Jackson, 1962; Cooperman, 1971; Jurewicz & Stock, 1976; Leonard, Mitchner & Self, 1980; Eschbach 1982; Kihm, Mitchner & Self 1985). Additional simplifications included uniform streamwise flow, constant Coulomb drift, and constant particle diffusivity. The predictions indicated that increased levels of particle diffusivity degrade ESP collection efficiency well below the hypothetical 'laminar' limit. Similar trends were predicted by Larsen & Sorenson (1984) and Yamamoto & Sparks (1985), who also considered the mean effects of the electric-wind secondary flow on particle collection. In each study, the mean secondary flow patterns were chosen in an *ad hoc* manner. For example, Larsen & Sorenson assumed a periodic, axial roll pattern superimposed upon a uniform streamwise velocity, while Yamamoto & Sparks assumed a sinusoidal variation in the streamwise flow streamlines near the collecting plate. Their results showed further reduction in efficiency due to these flow modifications. However, the success of these models is dubious since particle diffusivities must be empirically specified.

It is clear that a solid understanding of the electric wind and its role in electrostatic precipitation has not yet been established. Unexplainable observations, contradictory results, and unaddressed queries plague our current perception of this phenomenon. Attempts to accurately model particle dispersion and collection appear premature until the basic questions regarding the turbulent gas flow in precipitators are answered. The primary objective of this research was to establish an improved understanding of the turbulent gas flow resulting from the interaction of a corona-induced electric wind with the inlet flow of a precipitator. Of particular interest were the effects of current density, inlet velocity, and corona polarity on the mean and turbulent aspects of the gas flow. This research was carried out in a three-wire, parallel-plate electrostatic precipitator. The study consisted of three parts. First, flow visualization was performed to gain understanding of the physical processes involved in the electric-wind phenomenon. Second, fluid dynamic and electrostatic numerical models were developed to predict the model precipitator gas flow. While past experiments have revealed some three-dimensional behaviour (e.g. with negative polarity corona), the present models are two-dimensional because the major flow disturbances occur in the (x, y)-plane of the precipitator as shown in figure 2(*a*). Furthermore, a three-dimensional model would require a significant increase in computational time and memory, thereby placing a more severe constraint on the spatial resolution of each numerical solution. Thirdly, laser-Doppler anemometry was utilized to measure mean and turbulent gas velocities for model verification.

2. The model electrostatic precipitator

A model wire–plate electrostatic precipitator was chosen for conducting the experimental and numerical studies. The model precipitator consists of a pair of parallel conducting plates and an array of three equispaced wires located midway between the plates. This geometry with dimensional nomenclature is shown in figure 3. The actual dimensions are given in table 1.

Most dimensions were chosen to closely match those of a commercial ESP;

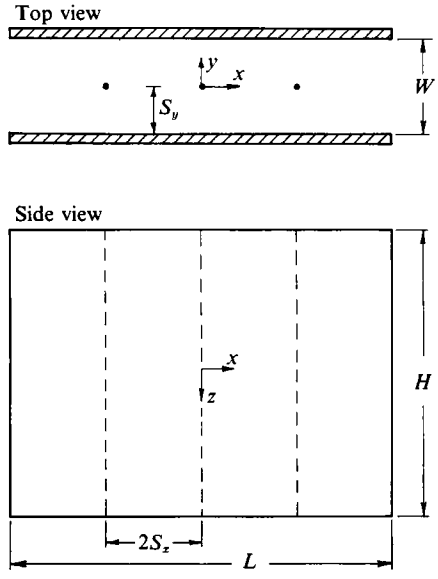

FIGURE 3. Model precipitator geometry.

Dimension	Symbol	Value
Length	L	81.28 cm (32 in.)
Height	H	60.96 cm (24 in.)
Width	W	20.32 cm (8 in.)
Wire–wire half-spacing	S_x	10.16 cm (4 in.)
Wire–plate spacing	S_y	10.16 cm (4 in.)
Wire radius	r_0	0.521 mm (0.0205 in.)

TABLE 1. Model precipitator dimensions

however, certain practical limitations exist. For example, wire–plate designs typically have a plate–plate spacing (width) of 20–30 cm (8–12 in.) and a wire–wire spacing of 15–30 cm (6–12 in.), but the height is often on the order of 6–9 m (20–30 ft). This yields height-to-width (aspect) ratios on the order of 30:1 which would be expensive to construct and cumbersome to test in a laboratory environment. Furthermore, the need to match the aspect ratio does not appear justified based upon past experimental investigations. Consequently, the chosen aspect ratio (3:1) represents an experimentally convenient design in which electrostatic and fluid dynamic end effects are sufficiently removed to allow the assumption of two-dimensionality. Discharge electrodes employed in commercial ESP units vary greatly in size and shape, depending upon plate–plate spacing, available power, corrosive nature of the gas, and the current folklore. A smooth wire electrode of 1.04 mm (0.41 in.) diameter was used in the present study.

The test section design utilized 9.5 mm ($\frac{3}{8}$ in.) thick Plexiglas endwalls to contain the gas flow and to provide insulating support for the corona discharge wires. Nichrome corona wires were used, which are relatively resistant to damage by sparking due to their high melting point. Each wire extended through nylon standoff insulators to anti-corona terminations consisting of a 2.5 cm (1 in.) diameter spherical aluminium ball at one end and a 2.5 cm (1 in.) diameter cylindrical

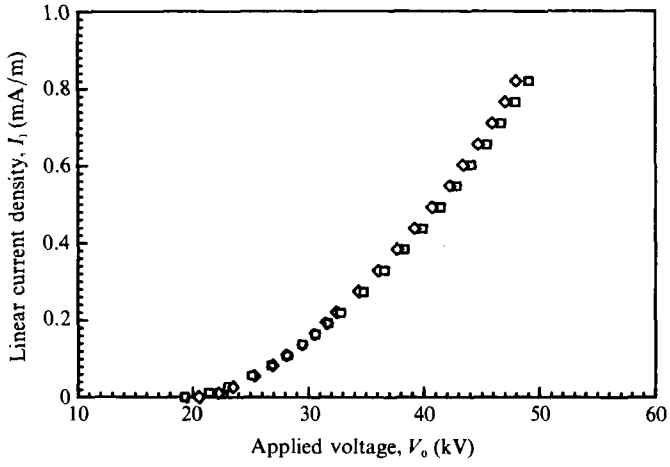

FIGURE 4. V–I characteristics of model precipitator: ◇, negative corona; □, positive corona.

Mean velocity m/s	R.m.s. velocity m/s	Turbulence intensity %	Flow uniformity %
1.96	0.0127	0.65	0.67
1.50	0.0152	1.01	—
1.01	0.0183	1.82	0.73
0.50	0.0132	2.64	1.18
0.30	0.0107	3.56	—

TABLE 2. Wind tunnel flow characteristics

aluminium bus bar at the other end. The nylon standoffs were threaded into the endwalls, thereby allowing the wires to be tensioned against the grip of setscrews in the anti-corona terminations.

An open-loop, blowing wind tunnel delivered a uniform, unidirectional flow of low turbulence to the model precipitator test section. Velocities within the test section were typical of industrial precipitators (U_0 = 1 to 2 m/s) and easily controlled by a guillotine valve. Flow characteristics 8 cm upstream of the test section are given in table 2. Further details of the wind tunnel design and performance are given in Kallio (1987).

The voltage–current (V–I) characteristics of the model precipitator are shown in figure 4. Note that negative polarity yields higher current and a higher starting voltage than positive polarity, which is typical of electrical coronas under standard temperature and pressure conditions (Cobine 1958). Operating currents of 0.2 and 0.5 mA/m were chosen, representing a moderate and high level, respectively.

3. Flow visualization

Flow visualization was performed in the model precipitator test section using smoke as a flow tracer. Smoke was introduced to the system at the inlet valve of the wind tunnel by vaporizing mineral oil in a pan heated by a rheostat-controlled hotplate. After passing through the blower and wind tunnel components, smoke entered the test section as a well-mixed, uniform tracer. Illumination was

accomplished by use of an Ar-ion laser light sheet formed by a cylindrical lens. The optics were configured so that both streamwise (x, y)- and spanwise (y, z)-planes could be visualized and recorded by still and video photography.

The visualization study was conducted over a range of inlet velocities (0 to 2 m/s) and linear current densities (0 to 0.5 mA/m) using positive and negative polarity. Upon energization, regions void of smoke were observed to form about each precipitator wire. The fate of these voids, as they convected downstream, served to indicate the extent of turbulent mixing within the precipitator core.

A significant feature was the existence of a critical value in inlet velocity (approximately 0.7 m/s), below which recirculation and turbulent mixing were widespread. In addition, there existed great differences between positive and negative polarity flow fields. The detailed results of the flow visualization study are reported in Kallio & Stock (1990), while the major observations are summarized below.

(i) Positive corona
  (*a*) Corona discharge is uniform and very stable for inlet velocities greater than 0.7 m/s, resulting in a two-dimensional flow with typical duct or pipe flow turbulence.
  (*b*) For velocities less than 0.7 m/s, the precipitator flow becomes unstable, exhibiting large circulatory cells that interact to produce widespread turbulence at the precipitator exit.

(ii) Negative corona
  (*a*) Corona discharge is inherently unsteady and three-dimensional, producing moderate turbulence for inlet velocities exceeding 0.7 m/s.
  (*b*) For velocities below 0.7 m/s, the precipitator flow behaves similarly to positive corona, displaying recirculating patterns with greatly increased turbulence.
  (*c*) Precipitator flow approaches a quasi-two-dimensional state for increased current density due to increased density of the discharge tufts.

4. Fluid dynamic modelling

Direct solution of the time-dependent Navier–Stokes equations is not yet economically feasible despite recent advances in computer technology and numerical techniques such as large-eddy simulation. Consequently, the most cost-effective way to solve practical turbulent flow problems is the use of statistically averaged equations governing the mean flow variables. These time-averaged equations contain correlations between fluctuating quantities (e.g. the Reynolds stresses) which must be closed by some turbulence model before the equations can be solved. This is the approach used in this study.

The electric wind is known to produce a recirculating secondary flow in many precipitator geometries which interacts with the inlet flow and developing plate boundary layer. Such a complex flow can contain various lengthscales that are difficult to prescribe or estimate. These attributes indicate that the least complex turbulence model required to analyse precipitator gas flows is a two-equation model. Furthermore, since the associated turbulence in precipitator gas flows may result from direct body force interaction, this complex flow could be a candidate for a second-order closure model. Fortunately, several geometrically similar recirculating flow problems have been modelled successfully with a k–ϵ formulation. These studies include the numerical simulation of a round jet in both unbounded and bounded

crossflow, performed by Patankar, Basu & Alpay (1977) and Jones & McGuirk (1980), respectively. Their predicted positions of the jet centreline show reasonable agreement with experimental data. Bernstein & Crowe (1981) employed the k–ϵ model in their preliminary investigation of the fluid dynamic field in wire–plate precipitators. Experimental measurements were not performed; however, gross qualitative agreement existed between laser-sheet flow visualization and the numerical results. Owing to these encouraging results and the expected difficulties associated with a second-order model, the k–ϵ turbulence model was selected to simulate the precipitator gas flow.

4.1. *Theoretical development*

The fluid dynamic model employed in the present study closely follows that described by Bernstein & Crowe (1981). The mathematical formulation consists of time-averaged mass and momentum conservation equations, combined with turbulence kinetic energy and turbulence dissipation transport equations. The gas flow is assumed steady, incompressible, two-dimensional and isothermal. The governing partial differential equations are listed below, where the coordinate system is the same as that shown in figure 3.

(i) Conservation of mass

$$\frac{\partial}{\partial x}(\rho\bar{u})+\frac{\partial}{\partial y}(\rho\bar{v}) = 0, \tag{1}$$

where ρ is the gas mass density, and $\bar{u}$, $\bar{v}$ are the mean streamwise and transverse velocity components, respectively. Since no mass sources exist, this equation of continuity represents a balance between the incoming and outgoing mass fluxes within a differential fluid volume.

(ii) Conservation of x- and y-momentum

$$\frac{\partial}{\partial x}\left(\rho\bar{u}^2-\mu_{\text{eff}}\frac{\partial\bar{u}}{\partial x}\right)+\frac{\partial}{\partial y}\left(\rho\bar{u}\bar{v}-\mu_{\text{eff}}\frac{\partial\bar{u}}{\partial y}\right) = -\frac{\partial\bar{p}}{\partial x}+f_{ex}, \tag{2}$$

$$\frac{\partial}{\partial x}\left(\rho\bar{u}\bar{v}-\mu_{\text{eff}}\frac{\partial\bar{v}}{\partial x}\right)+\frac{\partial}{\partial y}\left(\rho\bar{v}^2-\mu_{\text{eff}}\frac{\partial\bar{v}}{\partial y}\right) = -\frac{\partial\bar{p}}{\partial y}+f_{ey}, \tag{3}$$

where $\bar{p}$ is the mean gas pressure, μ_{eff} is the effective dynamic viscosity of the gas, and f_{ex}, f_{ey} are the electric body force density components in the streamwise and transverse directions, respectively. All dependent flow variables are assumed to consist of a mean and fluctuating component, i.e. $u = \bar{u}+u'$, $v = \bar{v}+v'$ and $p = \bar{p}+p'$. The terms on the left-hand sides of (2) and (3) represent momentum transport by convection and diffusion in the two coordinate directions. The right-hand-side terms are the forces exerted on the fluid volume. The body force term represents the momentum imparted to the gas by the corona-produced ion flux.

The proper formulation of the electric body force is obtained by considering the total electrical force acting on a group of free charges supporting a volumetric charge density ρ_f. This is given by the Lorentz force density (Panofsky & Phillips 1952),

$$\boldsymbol{f}_e = \rho_f \boldsymbol{E}+\boldsymbol{J}_f\times\boldsymbol{B}, \tag{4}$$

where $\boldsymbol{E}$ is the local electric field, $\boldsymbol{J}_f$ is the current density due to free charge motion and $\boldsymbol{B}$ is the local magnetic flux density field. In the electrostatic precipitator environment, the magnetic field force contribution is negligible owing to the low

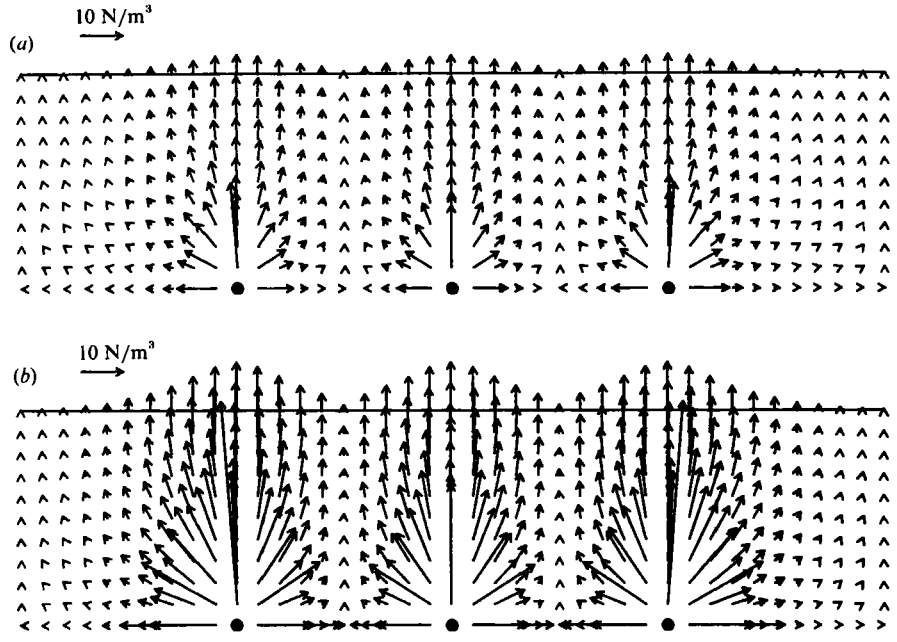

FIGURE 5. Prediction of electric body force field in model precipitator: (*a*) $V_0 = +32$ kV, $I_1 = 0.2$ mA/m; (*b*) $V_0 = +42$ *kV*, $I_1 = 0.5$ mA/m.

current densities available. Therefore, free charges, comprising a unipolar ion density, ρ_1, will only experience the Coulomb force,

$$\boldsymbol{f}_e = \rho_1 \boldsymbol{E}. \tag{5}$$

Equation (5) also represents the electrical force density acting on a ponderable medium (e.g. a fluid) if means are available for the force on the charges to be transmitted to the medium. For the situation of a gas in a precipitator, the flights of the ions are interrupted by collisions with neutral molecules that are in Brownian equilibrium. Since these collisions typically occur at frequencies much greater than the reciprocal times of interest (i.e. collisonal equilibrium is satisfied), complete momentum transfer takes place from the ion space charge to the fluid bulk (Melcher 1981). Therefore, the Coulomb force on the ions becomes an electric body force on the gaseous medium. This 'ion-drag' effect on the fluid is often considered an electrohydrodynamic (EHD) body force; however, it should be distinguished from those forces of direct electrical origin, such as dielectrophoresis or electrostriction (Pickard 1955).

Determination of the ion (space charge) density and electric field within the model precipitator requires numerical solution of Poisson's equation and the current continuity equation. This computation was accomplished by a combined finite-element, finite-difference method described in Kallio & Stock (1985) and Kallio (1987). In brief, quadratic elements are used to solve the electric potential field from Poisson's equation while first-order differencing of the continuity equation yields the space charge solution. The solution technique generally follows the iterative procedure of the Southern Research Institute (SRI) precipitator performance model (McDonald 1978).

Differences between positive and negative corona fields are included by specifying the appropriate ionic mobility while assuming a uniform current distribution in the

spanwise (z) direction. This assumption is justified for positive corona, but negative corona is known to produce discrete tufts of current along the discharge wire. This three-dimensional structure is most evident at lower current densities, where the tufts are widely spaced and irregular. Tuft density and uniformity increase with increasing current density. The two-dimensional electrostatic model used here is most appropriate for this latter condition.

Figure 5 shows predicted two-dimensional vector plots of the precipitator electric body force ($\rho_i \boldsymbol{E}$) for the model geometry at $V_0 = +32$ and $+42$ kV. These applied voltage values correspond to corona currents of 0.2 and 0.5 mA/m, respectively. Since values of ρ_i and $\boldsymbol{E}$ decrease rapidly away from the corona wire, a highly non-uniform force density exists. The magnitude of $\rho_i \boldsymbol{E}$ at the wire surface for $V_0 = +42$ kV is nearly 100 times greater than its magnitude at the collection plate opposite the wire, and is almost 1000 times greater than the value at the plate between wires. Negative-polarity body force results are slightly lower in magnitude ($< 10\%$) owing to the small difference in corona onset field, but the distribution is essentially identical.

The Boussinesq approximation is applied to relate the Reynolds turbulent shear stress term to the mean velocity gradients by use of a turbulent eddy viscosity (μ_t):

$$-\rho\overline{u'v'} = \mu_t\left(\frac{\partial \bar{u}}{\partial y}+\frac{\partial \bar{v}}{\partial x}\right). \tag{6}$$

The effective gas viscosity is thus the sum of the molecular viscosity (μ) and the turbulent viscosity, $\mu_{\text{eff}} = \mu+\mu_t$. The turbulent viscosity closure condition employed in the k–ϵ model is the Prandtl–Kolmogorov equation,

$$\mu_t = C_\mu \rho k^2/\epsilon, \tag{7}$$

where k is the turbulence kinetic energy, ϵ is the turbulence dissipation rate, and C_μ is an empirical constant. In two-dimensional flows, the kinetic energy and dissipation are usually defined by

$$k = \tfrac{3}{4}(\overline{u'^2}+\overline{v'^2}), \tag{8}$$

$$\epsilon = \frac{3\mu}{2\rho}\left[\left(\overline{\frac{\partial u'}{\partial x}}\right)^2+\left(\overline{\frac{\partial u'}{\partial y}}\right)^2+\left(\overline{\frac{\partial v'}{\partial x}}\right)^2+\left(\overline{\frac{\partial v'}{\partial y}}\right)^2\right]. \tag{9}$$

(iii) Conservation of turbulence kinetic energy:

$$\frac{\partial}{\partial x}\left(\rho\bar{u}k-\frac{\mu_{\text{eff}}}{\sigma_k}\frac{\partial k}{\partial x}\right)+\frac{\partial}{\partial y}\left(\rho\bar{v}k-\frac{\mu_{\text{eff}}}{\sigma_k}\frac{\partial k}{\partial y}\right) = G-\rho\epsilon, \tag{10}$$

(iv) Conservation of turbulence dissipation:

$$\frac{\partial}{\partial x}\left(\rho\bar{u}\epsilon-\frac{\mu_{\text{eff}}}{\sigma_\epsilon}\frac{\partial \epsilon}{\partial x}\right)+\frac{\partial}{\partial y}\left(\rho\bar{v}\epsilon-\frac{\mu_{\text{eff}}}{\sigma_\epsilon}\frac{\partial \epsilon}{\partial y}\right) = \frac{C_1\epsilon G}{k}-\frac{C_2\rho\epsilon^2}{k}, \tag{11}$$

where σ_k, σ_ϵ are effective Prandtl numbers for the diffusion of turbulence energy and dissipation, respectively, and C_1, C_2 are empirical constants. Details concerning the derivation of (10) and (11) and are described by Launder & Spalding (1974). The term G represents turbulence kinetic energy generation and is generally given by

$$G = \mu_{\text{eff}}\left\{2\left[\left(\frac{\partial \bar{u}}{\partial x}\right)^2+\left(\frac{\partial \bar{v}}{\partial y}\right)^2\right]+\left(\frac{\partial \bar{u}}{\partial y}+\frac{\partial \bar{v}}{\partial x}\right)^2\right\}. \tag{12}$$

The following standard values were used for the k–ϵ model constants: $C_\mu = 0.09$, $C_1 = 1.44$, $C_2 = 1.92$, $\sigma_k = 1.0$, $\sigma_\epsilon = 1.21$.

The possible direct contribution of turbulence kinetic energy or dissipation from the electric body force has been neglected in the previous formulation. If the electric body force or current density is considered a fluctuating parameter, i.e. $J = \bar{J} + J'$, then additional generation terms appear in the kinetic energy transport equation:

$$G_e = \frac{\overline{u' J'_x}}{b_i} + \frac{\overline{v' J'_y}}{b_i}, \tag{13}$$

where b_i is ionic mobility and J_x, J_y are the streamwise and transverse components of current density. Similar terms would also appear in the dissipation transport equation. Time-dependent fluctuations in current density due to variation in the space charge or electric field could arise from two sources. One source is the gas flow field, where ions might be locally transported by the turbulent fluid in a manner similar to the dispersion of fine particles or chemical species. This local ion density fluctuation, in turn, would cause a global fluctuation in the electric field, possibly in regions of the precipitator where the charge density is unaffected by the fluid. Furthermore, this electric field fluctuation would 'feed back' to the charge density field, and so on. Such a process might be described by control theory, serving to illustrate the tight coupling between the flow field, ion field, and electric field. The existence of this source of interaction in precipitators is doubtful in view of the high ionic velocities (50–100 m/s) in comparison to the turbulent velocity fluctuations. However, if particulate space charge were considered, such coupling would be more probable due to the relatively low mobility of particles.

A more likely source of time dependence in ion flux or electric field is that of electrostatic origin, where the corona process directly contributes to unsteadiness. Both polarities of corona are known to produce current fluctuations. For example, negative corona current is characterized by the *Trichel pulse* phenomenon. The frequency of these pulses for small electrode gaps is relatively high ($\sim$ 20 kHz), but decreases with applied voltage and gap distance (Kuffel & Zaengl 1984).

Generally speaking, it is not clear how significant electric turbulence generation or dissipation might be in view of the foregoing discussion. No model has yet been established for the terms in (13); however, Thomsen *et al.* (1982) suggested that they might be modelled by use of Prandtl's mixing-length arguments in a manner similar to buoyancy production terms in thermally stratified flows:

$$G_e \sim \mu_t (\nabla \rho_i \times \boldsymbol{E}). \tag{14}$$

Their estimates show that this term may be comparable to the turbulence generation by shear (G), especially near the discharge wires. In view of the fact that this model is untested and lacks a proportionality constant, electric turbulence generation has been neglected in the present study. Hence, all turbulence generation is attributed solely to shear in the mean flow.

The transport equations are modified near walls to account for the dominant viscous effects within the turbulent boundary layer. Consequently, the wall shear stress is required as a boundary condition for the momentum equations and for the evaluation of the kinetic energy generation term. This is accomplished by the so-called *wall-function* approach. This approach assumes that a constant shear stress exists within the viscous sublayer and, for points just outside, the velocity components parallel to the wall follow the logarithmic law of the wall. In addition,

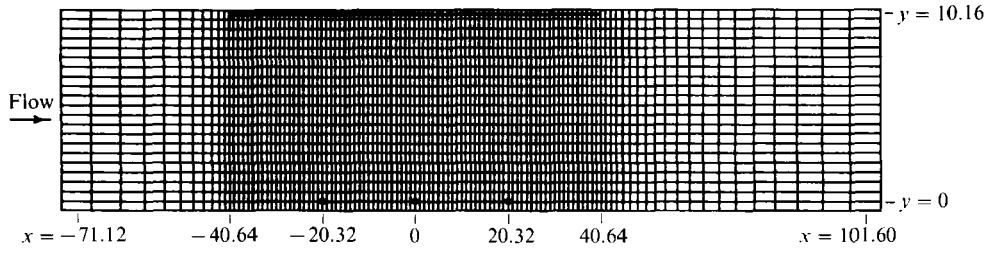

FIGURE 6. Fluid dynamic computational domain and finite-difference grid for model precipitator (units in cm).

the turbulence is assumed to be in local equilibrium, so that generation equals dissipation. With these assumptions, the resultant mean velocity parallel to the wall, kinetic energy, and dissipation rate at a point y from the wall can be related to the friction velocity U_τ by the following relations:

$$\bar{u} = \frac{U_\tau}{\kappa} \ln\left(\frac{A\rho U_\tau y}{\mu}\right), \tag{15}$$

$$k = U_\tau^2 / C_\mu^{\frac{1}{2}}, \tag{16}$$

$$\epsilon = U_\tau^3 / \kappa y, \tag{17}$$

where κ is Karman's constant and A is the logarithmic law of the wall constant, with assumed values of 0.4187 and 9.793, respectively.

4.2. *Solution method*

The governing fluid dynamic PDEs outlined above were solved using the TEACH-T numerical computer code, which was developed by Gosman & Pun (1973). The numerical method utilizes the hybrid finite-difference scheme to ensure stability. This scheme uses central differencing if the grid cell Péclet number is less than 2 and upwind differencing if the Péclet number is greater than 2. The cell Péclet number is a ratio of the strengths of convection and diffusion, defined as

$$Pe = \frac{|U|\Delta}{\Gamma_\phi}, \tag{18}$$

where U is the relevant fluid velocity, Δ is the grid cell width, and Γ_ϕ is the diffusivity of the transported property ϕ.

The finite-difference equations are solved on a staggered-point grid, where the pressure, kinetic energy, dissipation, charge density and electric field components are evaluated at the 'primary' nodes while the velocity components are defined at the midpoints between primary nodes. Solution convergence was tested by comparing the sum of all residual mass sources to the inlet mass flow rate. When this ratio became less than 0.01, the velocity values were invariant ($< 0.1\%$) between iterations.

The fluid dynamic computational domain and finite-difference grid for the model precipitator is shown in figure 6. Four boundaries enclose the domain: an inlet plane, an outlet plane, a symmetry plane along the wires, and a solid wall at the collecting plate. In general, boundary conditions need to be specified for the dependent variables at all these planes owing to the elliptic nature of the present flow problem. At the symmetry plane, the normal gradients of all variables are prescribed as zero,

and the velocity normal to the plane is also zero. At the solid wall, the normal velocity $\bar{v}$ is set to zero, while $\bar{u}$, k and ϵ are prescribed by the wall-function method described previously. The outlet plane was placed six wire–plate spacings downstream from the collecting plate edge, where the normal gradients of all variables were assumed zero.

The inlet plane boundary conditions are prescribed, as far as possible, from experimental measurements of the mean and fluctuating components of velocity. The streamwise mean velocity $\bar{u}_{\text{in}}$ was assumed uniform and the transverse mean velocity $\bar{v}_{\text{in}}$ was prescribed as zero. Uniform profiles were also prescribed for k and ϵ at the inlet plane, given by

$$k_{\text{in}} = \tfrac{3}{2}\overline{u'^2_{\text{meas}}}, \tag{19}$$

$$\epsilon_{\text{in}} = \frac{k_{\text{in}}^{\frac{3}{2}}}{0.02S_y}, \tag{20}$$

where $0.02S_y$ is the assumed lengthscale of the incoming turbulence (Gosman & Pun 1973).

Finite-difference grids of 72×12, 112×22, and 192×22 ($x \times y$) points were used. Uniform grid spacing was employed within the precipitator section and geometrically progressing grids (in the streamwise direction) were used in the inlet and outlet regions. The uniform cells were approximately 10 to 20 times larger than the corona wire radius for the grids considered, posing some difficulty in specifying the rapidly decaying electric body force. Consequently, volume-averaged electric body force values were utilized for the near-wire computations of $\bar{u}$ and $\bar{v}$. The problem of using a relatively coarse grid to approximate the near-singular body force is discussed further in the next section.

4.3. *Results and discussion*

Numerical predictions of the model precipitator gas flow field were obtained for inlet velocities ranging from 0.01 to 2.0 m/s and linear current densities of 0.2 and 0.5 mA/m. Only positive polarity was considered, since polarity had little effect on the predicted electric body force.

The predicted transverse profiles of streamwise velocity and turbulent kinetic energy opposite the centre corona wire ($x = 0$) were used to test the grid dependency of the computations. These results are shown in figure 7 for the three grid sizes, corresponding to an inlet mean velocity of 0.5 m/s and linear current density of 0.2 mA/m. Significant grid dependence is apparent in the kinetic energy predictions when the 72×12 grid was used. However, it appears that the profiles are approaching convergence for the 192×22 grid.

The observed grid dependence can be attributed to two sources. Firstly, the grid cell size is known to be relatively coarse in comparison to the rapid decay in electric body force near the discharge wires, as shown in figure 5. Consequently, the volume-averaging approach used here tends to 'wash-out' the details of the near-wire body force. Obviously, as finer grids about the wire are used, the body force becomes better approximated. The characteristic size of these gradients is on the order of the wire radius, which implies that grid spacing should be smaller than ~ 0.5 mm to adequately model the body force interaction in the vicinity of the wires. A uniform grid distribution of this size (1500×200) would be computationally expensive. The use of an adaptive grid or the finite-element technique might better accommodate this near-singular geometry.

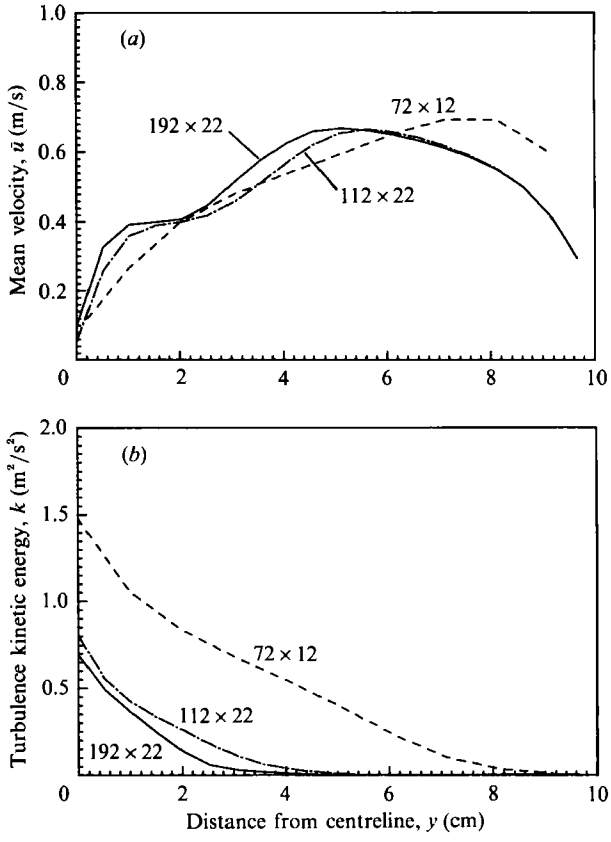

FIGURE 7. Grid dependency tests at $x = 0$ for $U_0 = 0.5$ m/s, $I_1 = 0.2$ mA/m ($V_0 = +32$ kV). (*a*) Mean streamwise velocity profile. (*b*) Turbulence kinetic energy profile.

The second feature contributing to grid dependence is false diffusion. Grid cell Péclet numbers ranged between 0.1 and 100, but were typically greater than 2 (convection-dominated). False diffusivity can be estimated for a two-dimensional flow problem by the following expression (de Vahl Davis & Mallinson 1972)

$$\nu_{\text{false}} = \frac{|U|\Delta x\,\Delta y \sin 2\theta}{4(\Delta y \sin^3\theta + \Delta x \cos^3\theta)}, \tag{21}$$

where Δx, Δy are the grid cell dimensions and θ is the angle made by the velocity vector with respect to the x-direction. Letting $\theta = 45°$, a maximum estimate of false diffusivity is obtained. For $U = 0.5$ m/s and $\Delta x = \Delta y = 0.5$ cm (192×22 grid), (21) yields a maximum diffusivity of approximately 9 cm^2/s. As will be seen later, this value is comparable to the predicted turbulent diffusivities. While grid dependence and false diffusion were not eliminated with a 192×22 grid, this size was deemed sufficient to provide a good qualitative description of the precipitator gas flow and to allow gross comparison with experimental data.

Figures 8–10 show mean velocity vector maps of the predicted gas flow within the precipitator section. The transverse scale (y-direction) of the maps has been enlarged by a factor of three with respect to the horizontal to allow better visualization. Figure 8(*a–c*), corresponding to $I_1 = 0.2$ mA/m, shows extreme examples of the electric-wind secondary flow which occurs at very low precipitator inlet velocities. At

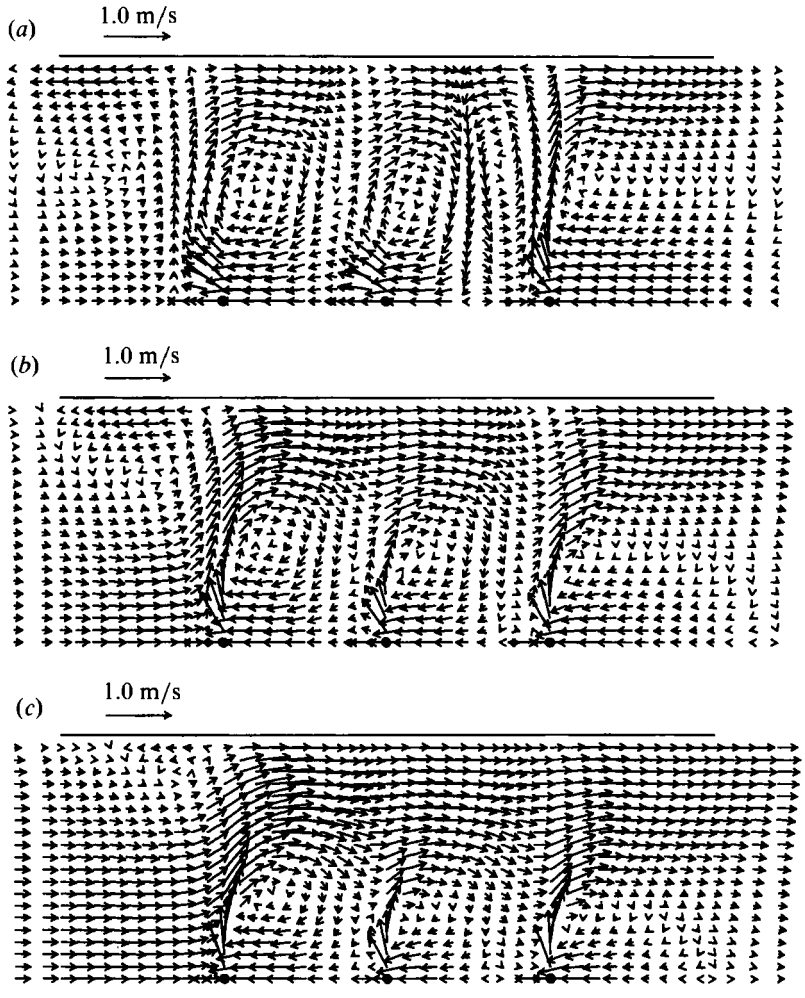

FIGURE 8. Mean velocity vector plots, $I_1 = 0.2$ mA/m ($V_0 = +32$ kV). (*a*) $U_0 = 0.01$ m/s, (*b*) 0.1 m/s, (*c*) 0.2 m/s.

the lowest velocity of 0.01 m/s, which can be considered a 'no-flow' precipitator, the electric wind produces pairs of circulatory cells, upstream and downstream of the wire. The peak transverse velocity opposite the wires for this case is 0.54 m/s, and -0.38 m/s between the wires. As the precipitator inlet velocity is increased, the crossflow causes the two circulatory cells between wires to merge into one, leaving a total of four cells. In addition, the peak transverse velocity opposite the wires increases and its location moves closer to the wire, while the velocity between the wires lessens.

Figure 9 (*a–c*) corresponds to precipitator inlet velocities of more practical interest. At $U_0 = 0.5$ m/s, the circulatory cell upstream of the first wire has disappeared, but recirculation still exists downstream of each wire. The flow visualization also displayed this behaviour. Further suppression of the circulatory patterns is seen at $U_0 = 0.7$ m/s, while at 1.0 m/s no recirculation is apparent and the electric-wind effect is restricted to the near-wire region. No significant perturbation of the flow field was predicted at $U_0 = 2$ m/s (not shown), which was also qualitatively supported by flow visualization. Interestingly, wallward transverse flow is greatest

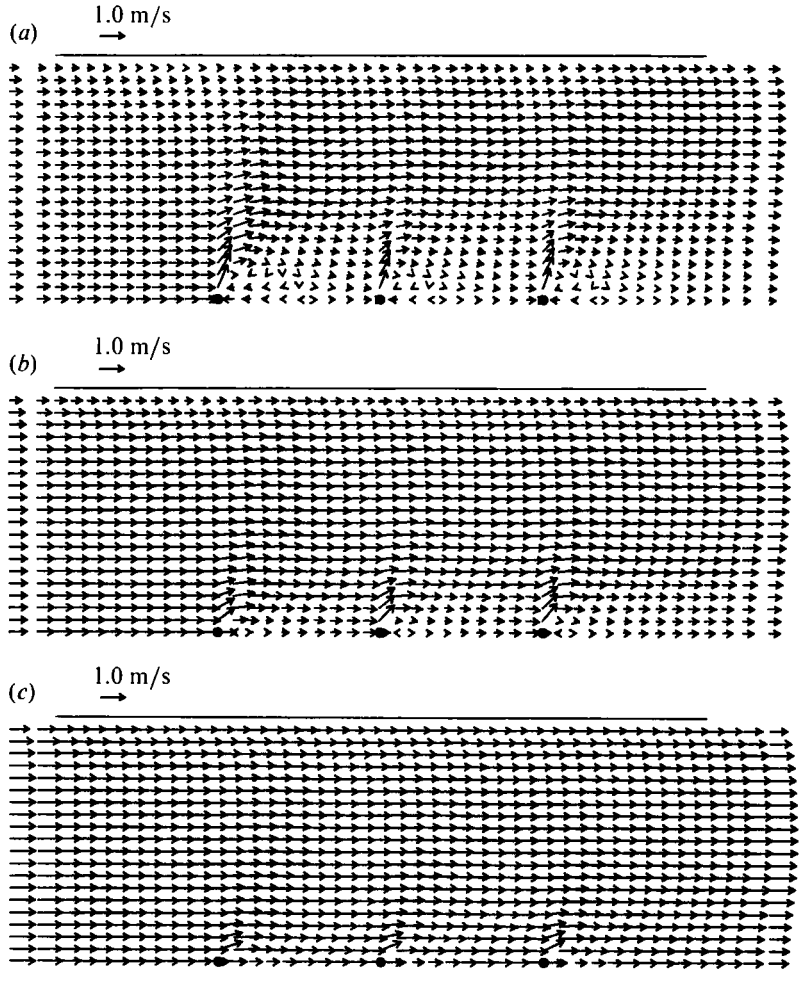

FIGURE 9. Mean velocity vector plots, $I_l = 0.2$ mA/m ($V_0 = +32$ kV). (*a*) $U_0 = 0.5$ m/s, (*b*) 0.7 m/s, (*c*) 1.0 m/s.

at $U_0 = 0.5$ m/s, where a peak velocity of 0.92 m/s was predicted near the wire. The transverse flow between wires, however, was relatively weak with velocities less than 0.1 m/s.

These series of vector maps give evidence for the importance of inlet velocity on the resulting gas flow patterns within wire–plate precipitators. The effect of corona current (or voltage) on the precipitator gas flow can be seen by comparing figures 8 and 9 with figure 10(*a–c*), where the linear current density has been increased to 0.5 mA/m. As expected, further perturbation of the gas flow field is predicted at higher I_l; however, the effect is not as dramatic as reducing U_0. Again, the highest transverse velocity occurred at $U_0 = 0.5$ m/s, where a peak value of 1.47 m/s was predicted.

Turbulent eddy diffusivity (μ_t/ρ) was computed by the TEACH-T code from (7). Diffusivity profiles (from duct centreline to plate) are given in figure 11 for $U_0 = 0.5$, 1.0 m/s and $I_l = 0.2$ mA/m at various positions along the precipitator length. Despite the absence of recirculation at $U_0 = 1.0$ m/s, significant diffusivity is predicted in the wire regions due to mean velocity shear. The shallow peak in

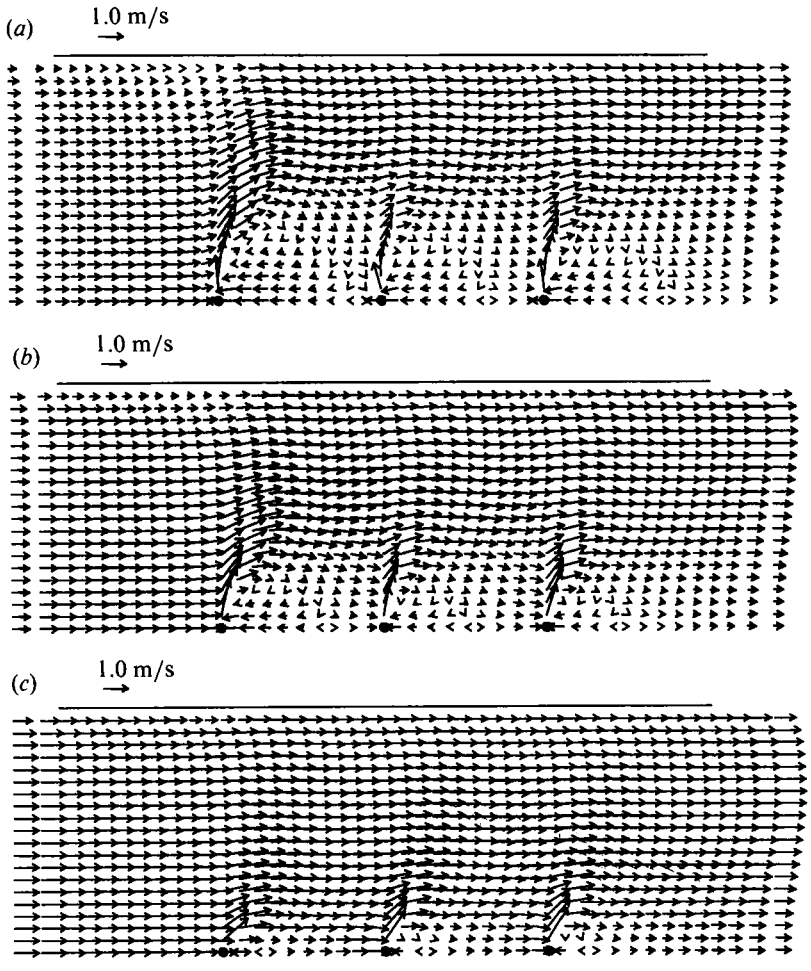

FIGURE 10. Mean velocity vector plots, $I_1 = 0.5$ mA/m ($V_0 = +42$ kV). (*a*) $U_0 = 0.5$ m/s, (*b*) 0.7 m/s, (*c*) 1.0 m/s.

predicted diffusivity near the collecting plate is due to normal boundary-layer growth. Further increases in wire region diffusivity are apparent at $U_0 = 0.5$ m/s due to recirculation. These plots show that the turbulent diffusivity of the precipitator gas flow generally increases with x, indicating that each energized wire adds turbulent energy to the flow in a cumulative fashion. These effects are important from the standpoint of particle dispersion and collection, which would be significantly influenced by the non-uniformity of these diffusivity profiles. The assumption of uniform particle diffusivity in a precipitator performance model does not appear valid based upon these findings. Figure 12 shows the strong effect of inlet velocity on the predicted turbulent diffusivity near the precipitator exit evaluated at $x = 30.48$ cm, $y = 0$.

In summary, a fluid dynamic–electrostatic numerical model has been used to predict the turbulent flow field in the model precipitator, the trends of which are supported by the previously described smoke flow visualization. Moreover, the parametric dependencies of U_0 and I_1 correspond to the findings of past studies. Quantitative comparisons between these predictions and experimental measurements are presented in the following section.

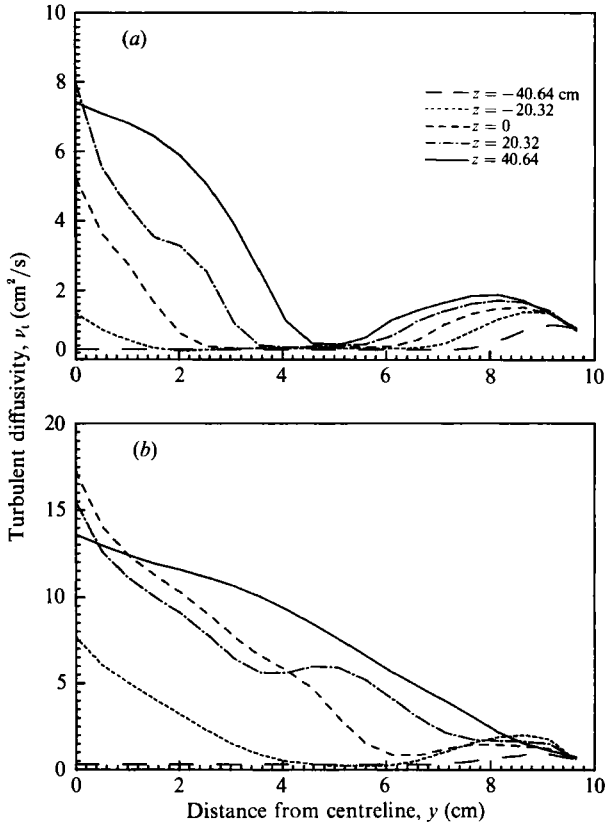

FIGURE 11. Turbulent diffusivity profiles at various x-locations, $I_1 = 0.2$ mA/m ($V_0 = +32$ kV). (*a*) $U_0 = 1.0$ m/s, (*b*) 0.5 m/s.

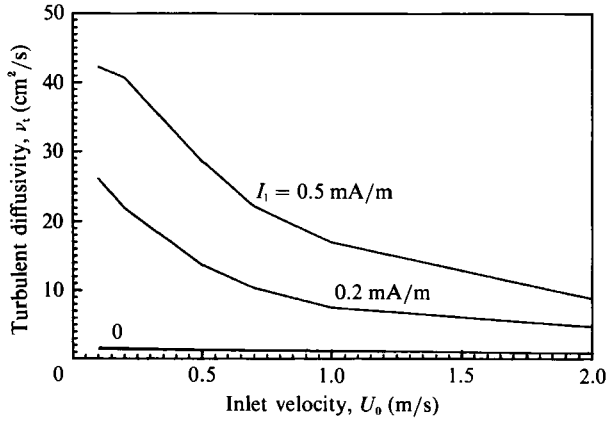

FIGURE 12. Turbulent diffusivity as a function of inlet velocity for various current densities at $x = 30.48$ cm, $y = 0$.

5. Laser-Doppler anemometry measurements

Experimental measurements using laser-Doppler anemometry (LDA) were performed to quantitatively characterize the turbulent gas velocity within the model electrostatic precipitator test section. Aside from characterizing the precipitator flow

	Blue (streamwise)	Green (transverse)
λ	488×10^{-9} m	514.5×10^{-9} m
$\frac{1}{2}\theta$	$1.541 \pm 0.001°$	$1.552 \pm 0.001°$
d_{mv}	0.18 mm	0.20 mm
l_{my}	5 mm	5 mm
f_s	10 kHz ($U_0 = 1.8$ m/s) 100 kHz ($U_0 = 1.0$, 0.5 m/s)	300 kHz (all velocities)

TABLE 3. Two-component LDA parameters (focal length = 600 mm)

field, these measurements were also used to evaluate the applicability of the fluid dynamic model. The non-intrusive nature of LDA allowed velocity measurements from seeded smoke particles inside the precipitator. The simultaneous, two-dimensional capability of the LDA system enabled determination of the turbulent Reynolds stress, $-\rho\overline{u'v'}$, in addition to the u- and v-components.

5.1. *Apparatus and procedure*

A Dantec (formerly DISA) three-beam, two-component LDA was used to measure the velocity of fine smoke particles within the precipitator test section. Separation of the two components of velocity was achieved by using the blue and green lines of the Ar-ion spectrum, provided by a Spectra-Physics model 164 laser (5 W continuous wave, all line). The Dantec 55X modular optics system provided the beam polarization, beam waist adjustment, beam splitting, frequency shifting, beam translations and beam focusing to produce a moving-fringe measuring volume of high spatial resolution. Doppler frequency shifting was employed to resolve velocity direction in reversing flows and to detect very low velocities. This was accomplished by use of a Bragg cell placed in the optical path of the laser beam, which was acoustically driven at 40 MHz by a Dantec 55N10 LDA frequency shifter. The same modular system also contained the backscatter components, consisting of a pinhole section, quartz mirror, photomultiplier (PM) optics and PM tubes. Operation of the anemometer in the backscatter mode allowed convenient mounting of the entire system on a three-dimensional traversing mechanism.

The LDA signal received by the photomultiplier/detector can be heuristically understood to result from light scattered by particles crossing interference fringes that are assumed to be located inside the measuring volume. This explanation, known as the fringe model, conveniently yields the relationship between particle velocity and Doppler frequency:

$$V_p = \frac{\lambda f_D}{2 \sin(\frac{1}{2}\theta)}, \tag{22}$$

where V_p is the seed particle velocity normal to the fringe plane, λ is the laser beam wavelength, f_D is the measured Doppler frequency and θ is the beam intersection angle. Table 3 gives the pertinent LDA parameters. The parameters d_{mv} and l_{mv} represent the approximate diameter and length, respectively, of the ellipsoidal measuring volume.

When frequency shifting is employed, the Doppler frequency in (22) is replaced by $(f_D - f_s)$, where f_s is the selected frequency shift of appropriate sign. Frequency shifts ranging from 10 to 300 kHz were used here, depending upon the precipitator inlet velocity (U_0) and the particular velocity component measured. Generally, signals

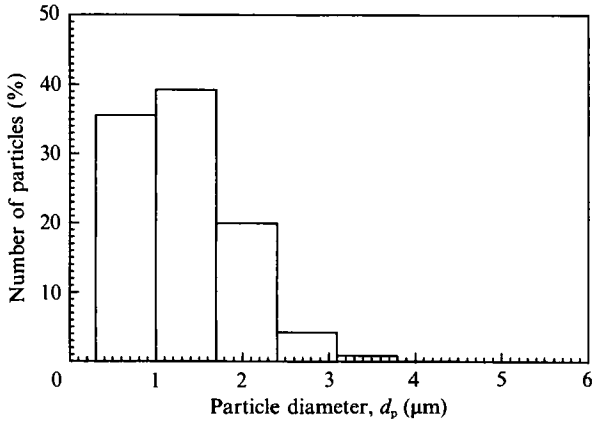

FIGURE 13. Size distribution (by number) of mineral oil smoke measured by laser aerosol spectrometer.

were shifted by an amount necessary to yield Doppler frequencies of at least 100 kHz so that they fell within the effective filter range of the counter processor. In addition, the signal shift was chosen high enough to prevent velocity 'rectification' due to flow reversal, normally satisfied by the first criterion. The shift frequencies were also chosen to produce a sufficient number of fringe counts to minimize incomplete signal bias (Stock & Fadeff 1983).

The seed particles used in the precipitator gas flow were generated by vaporizing mineral oil in a heated pan, similar to the method used in the flow visualization. For fluid velocity measurement the seed particles must be (i) small enough (of low inertia) to accurately track with the flow, yet (ii) large enough to scatter sufficient light for detection. The first requirement is normally satisfied by particles of low Stokes number ($St \ll 1$), which represents the ratio of particle inertia to the viscous drag experienced:

$$St = \frac{\rho_p d_p^2}{18\mu\tau_f}, \tag{23}$$

where ρ_p is particle mass density, d_p is particle diameter, and τ_f is the shortest timescale of interest within the flow. Typically, τ_f is determined by the ratio of the characteristic turbulent lengthscale to the r.m.s. fluctuating velocity. For the precipitator gas flow seeded with mineral oil droplets, particle diameters less than approximately 10 μm satisfy this criterion. The second requirement is dependent upon the available laser power and particular LDA optical geometry. For typical Ar-ion-based backscatter systems, velocity measurement of particles as small as 0.2–0.5 μm in diameter is feasible (G. Wigley 1984, personal communication).

The smoke generated was sized by a Particle Measuring Systems (PMS) model LAS-200 laser aerosol spectrometer, a 15-channel, sampling-type optical particle counter covering the size range of 0.3–10.8 μm diameter in fixed intervals of 0.7 μm. This instrument was factory calibrated with standard polystyrene latex (PSL) microspheres of various diameters, which have optical properties similar to mineral oil. The resulting size distribution based on number, sampled at the precipitator exit, is shown in figure 13. Greater resolution within the 0.3–2 μm size range is obviously needed for definitive sizing of this smoke; however, the entire distribution clearly falls below the 10 μm size limit. The calculated mean particle sizes, based upon diameter, surface area, and volume, are 1.3, 1.5 and 1.6 μm, respectively.

The LDA signals, or Doppler bursts, detected by the PM tubes were electronically mixed and shifted down to the selected frequency by a Dantec 55N10 frequency shifter. Processing of the signals was then accomplished by use of a Dantec 55L90a LDA counter processor for each colour. Once validated, the signals entered the Dantec 55G20 buffer interface, which provided communication between the counter processor and a PDP-11/23 microcomputer. Also included in this unit was the 57G149 coincidence filter board, which determined data coincidence from the blue and green signal channels to within a specified time window (typically 100 μs). This feature was used to compute the statistical correlation $\overline{u'v'}$, i.e. the turbulent Reynolds stress.

5.2. *Coulomb particle drift*

An important consideration regarding gas velocity measurement in electrostatic precipitators by LDA is the ubiquitous effect of Coulomb drift due to particle charging. This drift can contaminate the measurement, adding an electrical term to the local gas velocity, given by the following expression for particles of negligible inertia ($St \ll 1$):

$$V_p = U + b_p E, \tag{24}$$

where b_p is the electrical mobility of the seed particle, defined by (assuming Stokes' drag law is valid):

$$b_p = \frac{q_p}{3\pi\mu d_p}, \tag{25}$$

and q_p is the charge acquired by the particle. Particle charging in precipitators occurs when corona-generated ions attach to a particle. This process can occur by two mechanisms: (i) ion diffusion, and (ii) ion impaction due to the local electric field. The latter mechanism, known as field charging, is usually dominant in precipitators where $d_p \geqslant 0.5\,\mu\text{m}$. The high field charging rates in precipitators, characterized by the time constant $4\epsilon_0/\rho_i b_i$, typically allow particles to attain the saturation charge level (White 1953), given by

$$q_p = 3\pi\epsilon_0 d_p^2 E_0 \tag{26}$$

where E_0 is the maximum electric field strength encountered by a particle along its trajectory. Field charging calculations for the model precipitator show that a particle moving at 2 m/s acquires 90 % of its saturation charge within 3 cm in a uniform field with a negative ion charge density of 50 $\mu\text{C/m}^3$. This charge density represents an average value in the region between wire and plate at $I_1 = 0.5\,\text{mA/m}$. Therefore, the saturation charge assumption is reasonable in the model precipitator, especially at the lower inlet velocities. Equation (26) does not account for particle discharge, which rarely occurs in precipitators except at the collecting plate. It should be noted that this expression represents the saturation charge level of an electrically conducting particle, which is often a good assumption for vapour-generated particles owing to the likelihood of surface contamination (Inculet 1982).

To date, no general experimental method to decouple, or isolate, the terms in (24) has been successfully implemented. The fact that particles will always become charged in an ion field is virtually undeniable, so globally eliminating Coulomb drift is unlikely. However, there exist at least three other approaches to this problem.

One approach is to use seed particles that are sufficiently small so that Coulomb drift, $b_p E$, is negligible compared to U. This is certainly possible in some regions of the precipitator flow field, but in other regions, U may be very small or E very large

(e.g. near the wire). These regions are difficult to ascertain *a priori* since $\boldsymbol{U}$ is unknown. In addition, this approach could easily require an impractically small particle diameter, thereby precluding LDA measurement.

A second approach is to perform measurements where $\boldsymbol{E}$ and a component of $\boldsymbol{U}$ are known to be mutually perpendicular, thereby allowing direct measurement of that gas velocity component by the LDA. This method is obviously limited to symmetry planes within a wire–plate precipitator, namely, the transverse planes that intersect the wires and those that lie halfway between wires. Despite the regional limitations, this approach was employed to determine the streamwise mean gas velocities inside the model precipitator.

A third approach involves direct measurement of b_p and $\boldsymbol{E}$ at the points of interest in the flow field, thereby determining the Coulomb drift contribution. Such measurements would be very difficult to perform. Alternatively, the drift terms could be analytically evaluated from (25) and (26), yielding

$$b_p \boldsymbol{E} = \frac{\epsilon_0 d_p E_0 \boldsymbol{E}}{\mu}. \tag{27}$$

Since (26) represents a maximum particle charge, this drift calculation (when subtracted from the LDA-measured velocity) would yield conservative estimates of the local gas velocity. This approach was used to estimate the transverse mean gas velocities within the precipitator, where the electric field values were obtained from the finite-element, finite-difference electrostatic solution.

5.3. *Results*

Velocity measurements were primarily taken within one quadrant of the model precipitator, defined by the plane: $-40.54 < x < 0$ cm, $0 < y < 10.15$ cm, and $z = 0$. A three-dimensional traversing bench enabled velocity mappings and profiles to be taken over most of the quadrant with precision of ± 0.03 cm in the transverse (y) direction and ± 0.08 cm in the streamwise (x) and spanwise (z) directions. Owing to the anti-corona terminations, velocity measurements could not be performed within a 2 cm radius about the wires. In addition, measurements closer than 2 cm to the collecting plate were restricted by corner fillets.

Velocity measurement error was largely due to statistical uncertainties which can be quantified by 95% confidence intervals (Spiegel 1975). Based upon 1000 samples per data point, the confidence interval for mean velocity ($\bar{u}$) can be expressed as $\pm 5.2 u'_{\rm rms}/\bar{u}\%$. Typical values for $u'_{\rm rms}/\bar{u}$ ranged between 0.01 and 0.4. Confidence intervals for r.m.s. velocities can be approximated by $\pm 4.4 u'_{\rm rms}/\bar{u}\%$.

Transverse profiles of the streamwise component of mean velocity ($\bar{u}$) were measured at three stations within the precipitator. These stations, or positions, correspond to $x = -20.32$ cm (position '1', opposite the first wire), $x = -10.15$ cm (position '2', between first and second wire), and $x = 0$ (position '3', opposite the second wire). The $x = 0$ position is an electrostatic symmetry axis where $E_x = 0$. Furthermore, results from the electrostatic model show that $E_x = 0$ along $x = -10.15$ cm is also a good approximation. The approximation is not strictly warranted at $x = -20.32$ cm; however, the ratio of electric field components is still relatively low, $E_x/E_y \approx 0.05$. Consequently, all three profile positions can be considered symmetry axes, where the streamwise gas velocity is decoupled from Coulomb drift since $b_p E_x \approx 0$.

The measured streamwise mean velocity profiles along the symmetry lines are shown in figures 14–16 for positive and negative polarity at $U_0 = 0.5$, 1.0 and 1.8 m/s.

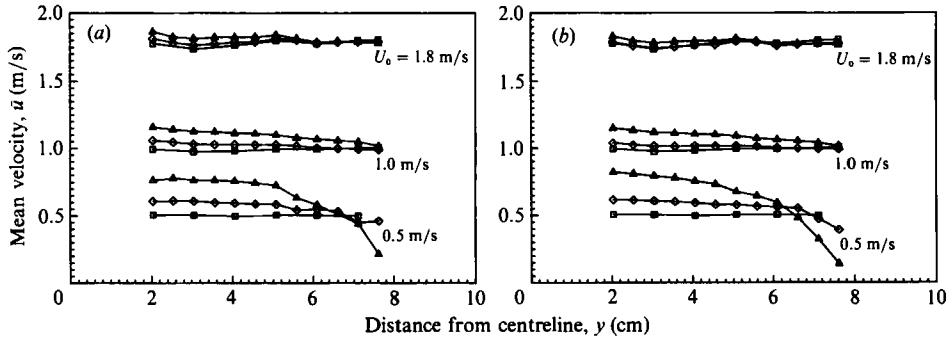

FIGURE 14. Streamwise mean velocity profiles at position 1: (*a*) positive corona, (*b*) negative corona, □, $I_1 = 0$ mA/m; ◇, 0.2 mA/m; △, 0.5 mA/m.

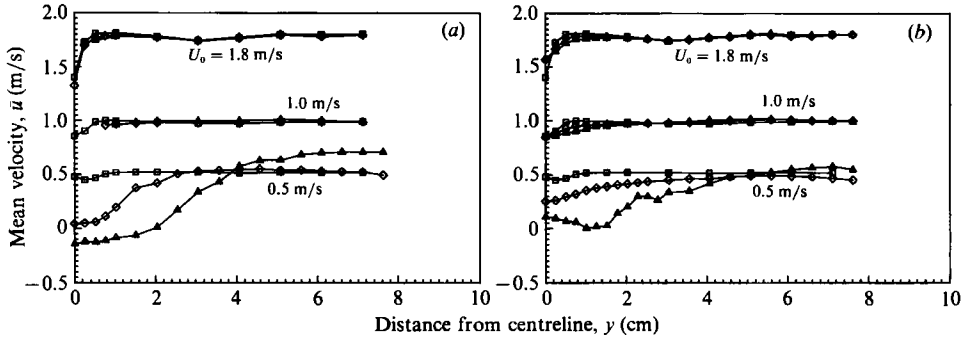

FIGURE 15. Streamwise mean velocity profiles at position 2: (*a*) positive corona, (*b*) negative corona, □, $I_1 = 0$ mA/m; ◇, 0.2 mA/m; △, 0.5 mA/m.

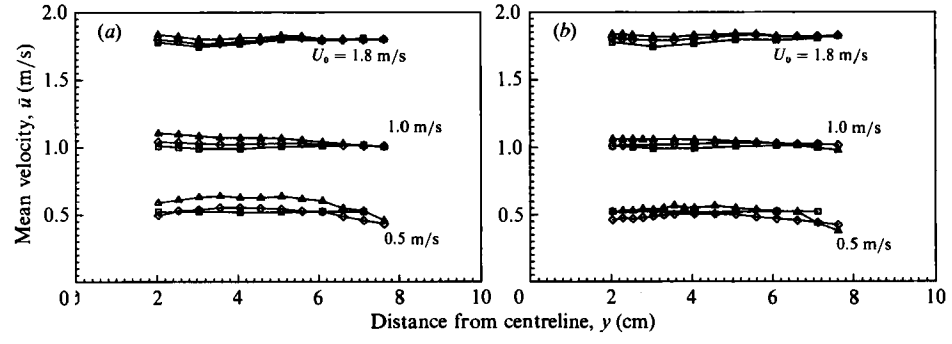

FIGURE 16. Streamwise mean velocity profiles at position 3: (*a*) positive corona, (*b*) negative corona, □, $I_1 = 0$ mA/m; ◇, 0.2 mA/m; △, 0.5 mA/m.

In general, negligible polarity dependence is evident. The flow perturbations due to the electric wind are most apparent at 0.5 m/s; however, significant effects still occur at 1.0 m/s. The effects of electric wind at $U_0 = 1.8$ m/s are entirely suppressed. At position 1, the flow increases within the core region, replacing the rapid ejection of gas near the first wire due to the dominant electric wind. This acceleration in core velocity was also detected upstream of the first wire. Continuity demands a decrease in flow near the plate, which is also apparent in the profiles. In extreme cases of low inlet velocity, the flow deceleration near the plate caused recirculation, as predicted

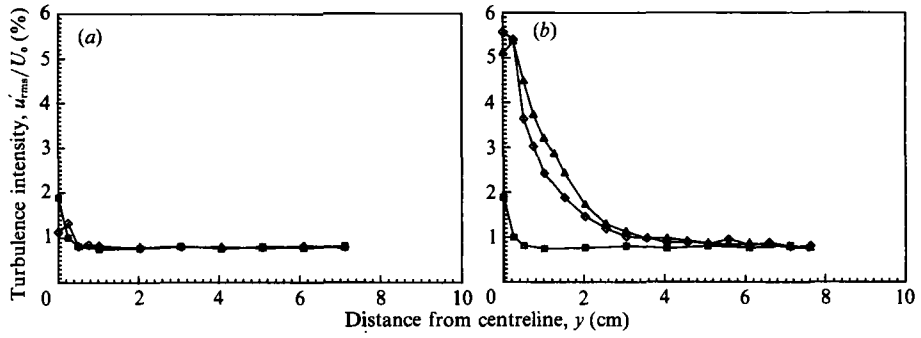

FIGURE 17. Streamwise turbulence intensity profiles at position 2 for $U_0 = 1.8$ m/s: (*a*) positive corona, (*b*) negative corona, □, $I_1 = 0$ mA/m; ◇, 0.2 mA/m; △, 0.5 mA/m.

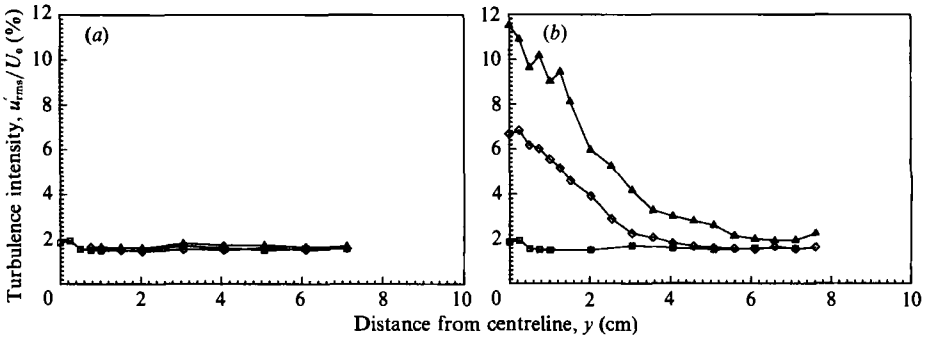

FIGURE 18. Streamwise turbulence intensity profiles at position 2 for $U_0 = 1.0$ m/s: (*a*) positive corona, (*b*) negative corona, □, $I_1 = 0$ mA/m; ◇, 0.2 mA/m; △, 0.5 mA/m.

by the fluid dynamic model. These measurements are in general agreement with the numerical predictions of Yamamoto & Velkoff (1981) and the LDA measurements of Leonard *et al.* (1983). At position 2, the measured profiles for $U_0 = 0.5$ m/s are nearly opposite to those at position 1, showing flow reversal downstream of the wire and flow acceleration near the collecting plate. The latter observation has implications for precipitator performance, where increasing flow near the plate may promote particle re-entrainment. Again, this is consistent with smoke flow visualization and the TEACH-T velocity vector plots. The flow deficit in the wire wake region is apparent for $U_0 = 1.0$ and 1.8 m/s. The effects of electric wind at position 3 were surprisingly negligible, even at low inlet velocity. This is attributed to the mixing of secondary flows generated by the first and second wires. This interaction yields high turbulence levels, which is thought to promote enough momentum transport to effectively 'smooth out' the measured mean velocity profile.

Profiles of streamwise r.m.s. fluctuating velocity are presented in figures 17–19 for both corona polarities, measured at position 2. These plots show that significant differences exist between positive and negative corona in terms of turbulence generation. Positive-corona measurements show very little streamwise turbulence for inlet velocities of 1.0 and 1.8 m/s at all positions (see figures 17 and 18). In contrast, significant turbulent character is displayed in the negative-polarity profiles, even at 1.8 m/s. This is strongly supported by the laser-sheet flow visualization, where the negative discharge was characteristically unsteady at all

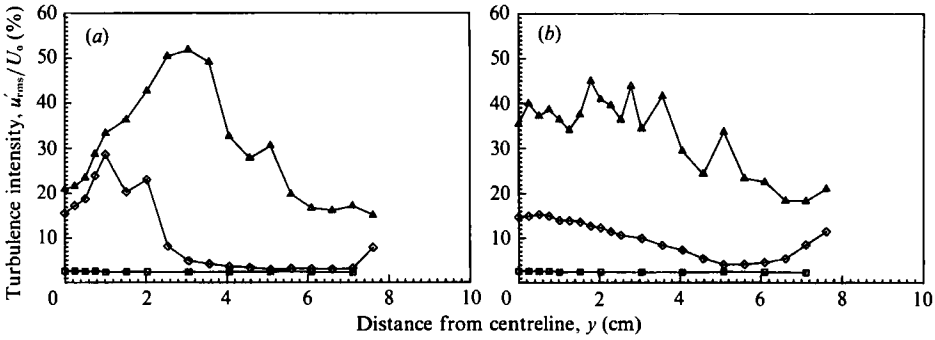

FIGURE 19. Streamwise turbulence intensity profiles at position 2 for $U_0 = 0.5$ m/s: (*a*) positive corona, (*b*) negative corona, □, $I_1 = 0$ mA/m; ◇, 0.2 mA/m; △, 0.5 mA/m.

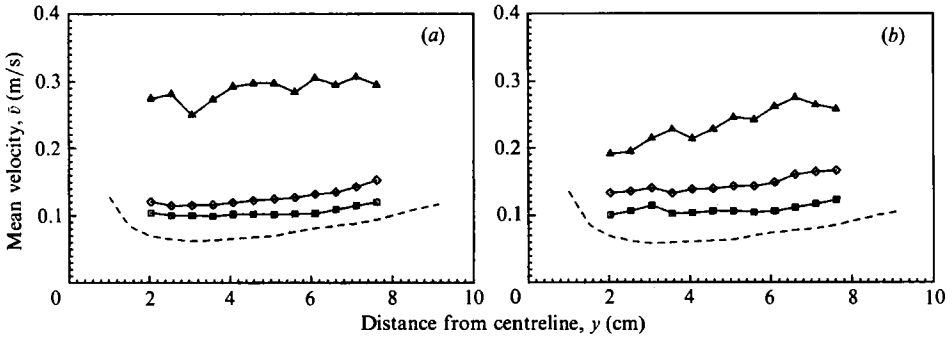

FIGURE 20. Transverse mean velocity profiles at position 1 for $I_1 = 0.5$ mA/m: (*a*) positive corona, (*b*) negative corona, □, $U_0 = 1.8$ m/s; ◇, 1.0 m/s; △, 0.5 m/s; ----, estimated Coulomb drift.

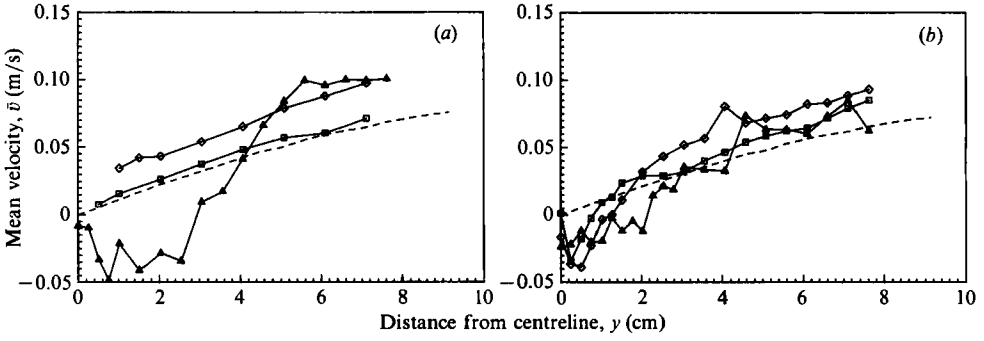

FIGURE 21. Transverse mean velocity profiles at position 2 for $I_1 = 0.5$ mA/m: (*a*) positive corona, (*b*) negative corona, □, $U_0 = 1.8$ m/s; ◇, 1.0 m/s; △, 0.5 m/s; ----, estimated Coulomb drift.

inlet velocities while positive discharge was relatively stable for $U_0 > 0.7$ m/s. The turbulence intensity profiles corresponding to $U_0 = 0.5$ m/s (figure 19) show very high values for both polarities owing to the presence of recirculation. Turbulence profiles at positions 1 and 3 were also measured (not shown), showing very similar effects with regard to polarity dependence.

Transverse mean and r.m.s. velocities were measured at positions 1, 2 and 3 for both polarities. Mean velocity profiles at $I_1 = 0.5$ mA/m are shown in figures 20–22 for the various inlet velocities. In order to interpret the electric-wind effects, an

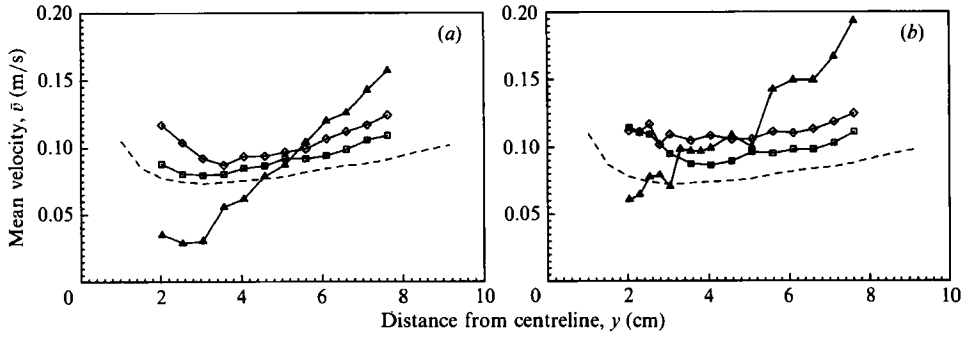

FIGURE 22. Transverse mean velocity profiles at position 3 for $I_1 = 0.5$ mA/m : (*a*) positive corona, (*b*) negative corona, □, $U_0 = 1.8$ m/s; ◇, 1.0 m/s; △, 0.5 m/s; ----, estimated Coulomb drift.

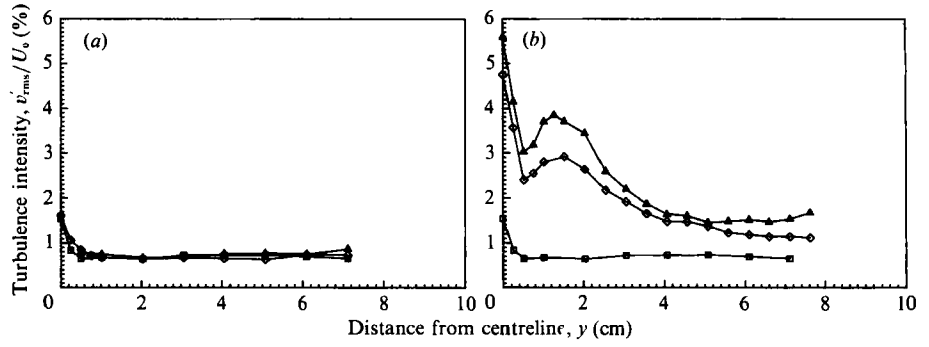

FIGURE 23. Transverse turbulence intensity at position 2 for $U_0 = 1.8$ m/s: (*a*) positive corona, (*b*) negative corona, □, $I_1 = 0$ mA/m; ◇, 0.2 mA/m; △, 0.5 mA/m.

estimate of Coulomb particle drift from (27) is plotted in these figures. The value of E_0 used in (27) is assumed to correspond to the local electric field for position 1 estimates. For positions 2 and 3, E_0 is taken as the average field opposite the first wire.

In figure 20, corresponding to position 1, the Coulomb drift estimates roughly correspond to the measured velocity profile at $U_0 = 1.8$ m/s, indicating negligible flow perturbation. At the lower inlet velocities, significant discrepancies abound which are attributed to an additional transverse component in gas velocity from the electric wind. In contrast, the profiles at position 2 in figure 21 display negative transverse velocities near the duct centre, which becomes positive and increase toward the collecting plate. This behaviour occurs for all negative-polarity cases, but is only evident at $U_0 = 0.5$ m/s for positive polarity. By comparison to the estimate of Coulomb drift, it is obvious that the gas flow has been perturbed by electric wind at the lowest inlet velocity condition. These profiles indicate recirculation, where the electric wind promotes a weak return flow toward the duct centreline. The velocity profiles at position 3 in figure 22 are more difficult to interpret, considering the differences between these measurements and those of position 1. It again appears that negative transverse gas velocities are present here for $U_0 = 0.5$ m/s, possible due to the interaction of the recirculating flows generated by both wires.

The measured transverse components of r.m.s. fluctuating velocity (turbulence intensity) are presented in figures 23–25 for position 2. Again, negligible velocity

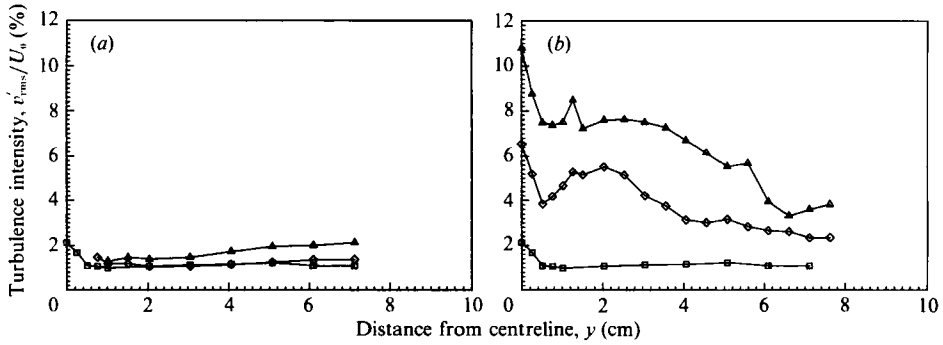

FIGURE 24. Transverse turbulence intensity at position 2 for $U_0 = 1.0$ m/s: (*a*) positive corona, (*b*) negative corona, □, $I_1 = 0$ mA/m; ◇, 0.2 mA/m; △, 0.5 mA/m.

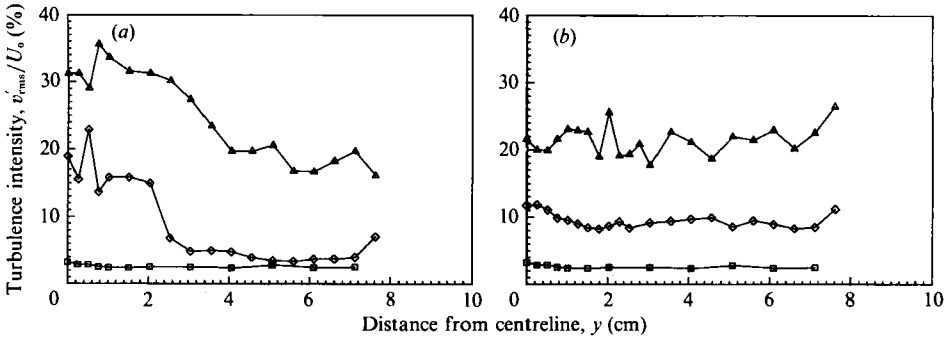

FIGURE 25. Transverse turbulence intensity at position 2 for $U_0 = 0.5$ m/s: (*a*) positive corona, (*b*) negative corona, □, $I_1 = 0$ mA/m; ◇, 0.2 mA/m; △, 0.5 mA/m.

fluctuation was measured for positive corona at 1.0 and 1.8 m/s inlet velocity (figures 23 and 24). Aside from representing little turbulence generation, this feature also indicates negligible fluctuation in Coulomb drift, i.e. constant particle electrical mobility. This observation is rather surprising, considering the polydisperse nature of the smoke size distribution. Such behaviour can be partially attributed to LDA particle size bias – the rejection of small burst signals (< 200 mV in amplitude) by the counter processor. These rejected signals represent smaller particles on the average, thereby biasing the measurement toward higher mean velocity and lower r.m.s. values. The existence of near-constant seed particle mobility is fortunate from the standpoint that it allows direct analysis of the transverse r.m.s. contribution of electric wind. These plots are similar to those of streamwise turbulence intensity with regard to polarity dependence, further supporting the contention that negative corona produces significant turbulence at all inlet velocities considered, whereas positive corona only shows turbulence generation at $U_0 = 0.5$ m/s (figure 25). The streamwise and transverse fluctuating velocities also have similar profile trends, but close inspection reveals a certain degree of anisotropy. This is especially evident for negative corona, where the level of anistropy, u'_{rms}/v'_{rms} ranges in value from approximately 0.3 to 0.5 over a significant portion of the precipitator at inlet velocities of 1.0 and 1.8 m/s. At $U_0 = 0.5$ m/s, anisotropy levels of ~ 2 are revealed for both corona polarities, indicating a significant change in the nature of the turbulence produced.

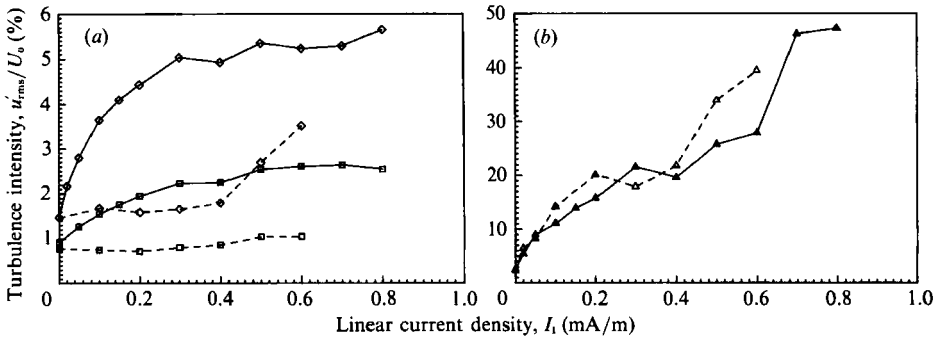

FIGURE 26. Streamwise turbulence intensity as a function of linear current density near precipitator exit ($x = 30.48$ cm), (*a*) $U_0 = 1.8$ m/s (□), 1.0 m/s (◇); (*b*) 0.5 m/s, ----, positive corona; —, negative corona.

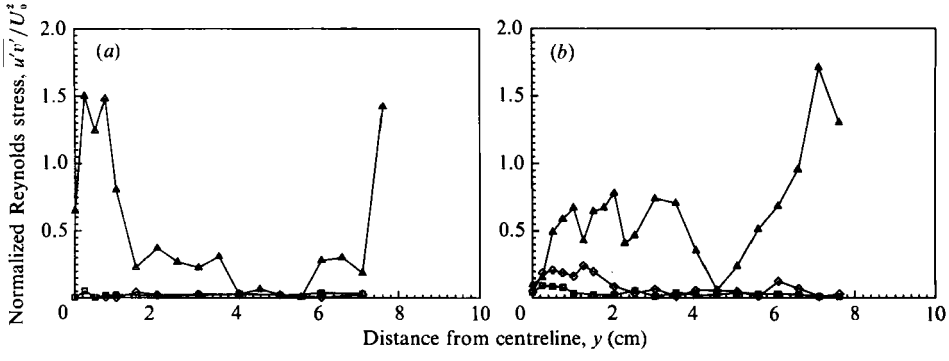

FIGURE 27. Reynolds stress profiles at position 2 for $I_1 = 0.2$ mA/m; (*a*) positive corona, (*b*) negative corona. □, $U_0 = 1.8$ m/s; ◇, 1.0 m/s; △, 0.5 m/s.

The effect of linear current density on streamwise turbulence intensity near the precipitator exit is shown in figure 26. These plots support the foregoing observations of a threshold phenomenon in inlet velocity and the polarity dependence of the turbulence at higher inlet flows. Turbulence intensity is seen to saturate with increased current for $U_0 > 1.0$ m/s but increases in a near-linear fashion for $U_0 = 0.5$ m/s.

The Reynolds stress measurements performed by the two-component LDA are shown in figure 27, corresponding to a current density of 0.2 mA/m with both polarities. Very significant turbulent stresses were measured at an inlet velocity of 0.5 m/s, which is not unexpected from previous results. In general, the greatest stress contributions are seen in the mid-duct and collecting-plate regions. This trend is consistent with the TEACH-T turbulent eddy diffusivity predictions.

5.4. *Comparison with model predictions*

Qualitative agreement has been shown to exist between the LDA-measured mean velocities and the fluid dynamic (TEACH-T) vector plots. A quantitative comparison between the TEACH-T predictions and the LDA mean velocity measurements is shown in figure 28. An inlet velocity of 0.5 m/s was chosen since this condition yields a significant mean flow perturbation. Streamwise velocity profiles are plotted for positions 1 and 2 under the influence of positive corona. The predictions are shown to match the trends in the data, with most discrepancy occurring in the mid-duct

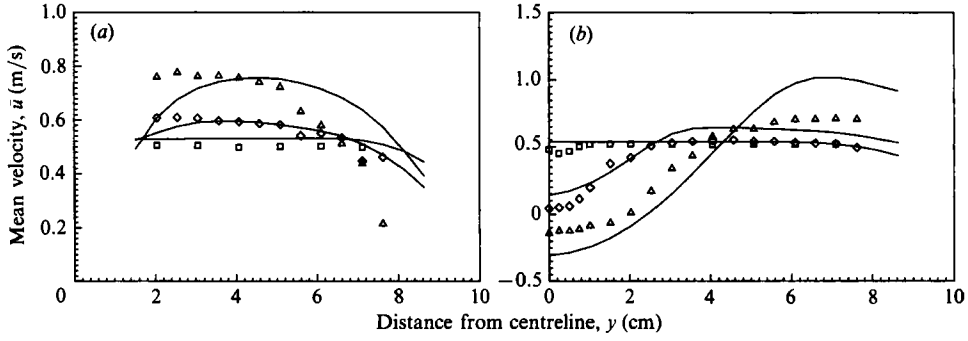

FIGURE 28. Comparison of LDA-measured streamwise mean velocity profiles (positive corona) (□, $I_1 = 0$ mA/m; ◇, 0.2 mA/m; △, 0.5 mA/m) with TEACH-T predictions (—) for $U_0 = 0.5$ m/s; (*a*) position 1, (*b*) position 2.

(wire) and plate regions. This probably reflects the coarseness of the 192 × 22 grid in relation to the velocity gradients present in these regions. Considering the grid deficiencies and the empirical nature of the turbulence model, these predictions are very encouraging. Comparison between predicted and measured turbulence kinetic energy (not shown) displayed much poorer agreement; however, the trends were consistent in that the highest values of kinetic energy were predicted near the wire and plate, respectively. Such differences between model predictions and data are not unusual, as evidenced in similar turbulence studies, e.g. the impingement of a jet in crossflow (Barata, Durao & Heitor 1985). The precise cause of the discrepancies is difficult to identify, since they may be attributable to numerical and/or turbulence modelling errors.

6. Conclusions and discussion

The turbulent gas flow known as electric wind resulting from the interaction of electrostatic and fluid dynamic fields in a wire–plate precipitator has been characterized for a particular model geometry over a range of operating conditions. The results show that the electric wind exists as a very complex flow phenomenon which is strongly dependent upon corona polarity and precipitator inlet velocity. The flow visualization and LDA results support the major findings of past investigations but provide a more lucid and detailed description of the electric wind. The two-dimensional fluid dynamic model, based upon the TEACH-T computational code and coupled with an improved electrostatic model, is useful in predicting some of the important features of the precipitator gas flow. The following list summarizes the specific conclusions drawn from this investigation.

(i) The dominance of electric wind and associated secondary flows in wire–plate precipitators is very sensitive to the magnitude of inlet velocity. The presence of inlet flow (crossflow) causes suppression of the secondary flow field in a sudden manner characterized by a threshold velocity. For the particular geometry investigated, it was found from flow visualization that this threshold point occurs near 0.7 m/s and is relatively insensitive to linear current density. Inlet velocities above this value exhibited negligible mean flow perturbation by the electric wind. For precipitator inlet velocities less than the threshold value, gas recirculation prevailed for both polarities of corona where the extent of recirculation was roughly proportional to current. Strong evidence of turbulent dispersion and large-scale mixing was evident

for these low-inlet-velocity situations. The two-component LDA measurements revealed high values of streamwise and transverse turbulence intensities below threshold, typically 40–50% based upon inlet velocity.

(ii) The turbulence produced by the electric wind is neither homogeneous nor isotropic. This characteristic was evident from the turbulence intensity and Reynolds stress measurements by LDA. At above-threshold inlet velocities, negative corona turbulence possessed anisotropy levels of ~ 0.4, whereas values of ~ 2 were measured below threshold for both polarities. Such differences indicate that the turbulence generated by the unsteady negative corona discharge above threshold is much different than the turbulence associated with the recirculation that occurs below the threshold velocity.

(iii) The TEACH-T fluid dynamic model is useful for qualitative prediction of the electric-wind gas flow field and has the potential of becoming a reasonable quantitative tool, with some improvement. This improvement primarily entails grid refinement. The difficulty in attaining grid independence was attributed to the near-singular nature of the electric body force. In order to accurately specify the near-wire body force, finer computational grids about the discharge wire will be required. This would also reduce numerical diffusion, which was significant in some regions of the computational domain. Despite the numerical inadequacies, the fluid dynamic model predicted the existence of secondary flows, consistent with the smoke flow visualization and LDA measurements. The effect of increased corona current was shown to cause more extensive recirculation and higher turbulent diffusivity. The suppression of recirculation and turbulence with increasing precipitator inlet flow was also clearly predicted. However, the model was unable to predict the differences in turbulence generation between positive and negative corona. This deficiency is attributed to the assumed steady and two-dimensional behaviour of the electrostatic and fluid dynamic fields. These assumptions are valid for the stable, uniform positive corona, but are probably unrealistic for negative corona. In order to properly predict negative-corona electric wind, some source of unsteadiness must be incorporated into the model. In addition, the three-dimensional behaviour of negative corona may be significant; however, this inclusion may not be crucial for moderate to high current densities where the discharge becomes more uniform along the wire length.

We thank J. R. Ferguson for his assistance with the LDA and for many hours of discussion, R. A. Lentz for his help with electronics troubleshooting and microcomputer data acquisition/processing and T. D. Hellesto and the College of Engineering Shop for their craftsmanship. We also thank Ms. J. Rattey-Hicks for typing the manuscript. Support from the US Department of Energy in the form of a research fellowship and a summer research assistantship from Washington State University are gratefully acknowledged.

REFERENCES

Barata, J. M. M., Durao, D. F. G. & Heitor, M. V. 1985 Experimental and numerical study on the aerodynamics of jets in ground effect. *Tenth Symp. on Turbulence, University of Missouri, Rolla, MO, Paper* 34.

Bernstein, S. & Crowe, C. T. 1981 Interaction between electrostatics and fluid dynamics in electrostatic precipitators. *Environ. Intl* **5**, 181–189.

Cobine, J. D. 1958 *Gaseous Conductors – Theory and Engineering Applications.* Dover.

Cooperman, P. 1971 A new theory of precipitator efficiency. *Atmos. Environ.* **5**, 541–551.

COTTRELL, F. G. 1914 Problems in smoke, fume and abatement. *US Govt Printing Office, Publication 2307*, pp. 553–585.

DAVIDSON, J. H. 1984 Secondary flows and turbulence in electrostatic precipitators. Ph.D. dissertation, Duke University.

DEUTSCH, W. 1922 Bewegung und Ladung der Elektricitatstrager in Zylinder Kondensator. *Ann. Phys.* **58**, 335–344.

ESCHBACH, E. J. 1982 Numerical prediction of electrostatic precipitator performance. MS thesis, Washington State University.

FLIPPEN, L. D. 1982 Electrohydrodynamics. Ph.D. dissertation, Duke University.

GOSMAN, A. D. & PUN, W. M. 1973 Calculation of recirculating flows. *Lecture Notes, Imperial College of Science and Technology.*

INCULET, I. 1982 Particle charging in dc corona fields. *IEEE Trans. Electric. Insul.*, **EI-9**, 158–191.

JONES, W. P. & MCGUIRK, J. J. 1980 Computation of a round turbulent jet discharging into a confined cross flow. In *Turbulent Shear Flow 2* (ed. L. Bradbury *et al.*), pp. 233–245. Springer.

JUREWICZ, J. T. & STOCK, D. E. 1975 A numerical model for turbulent diffusion in gas-particle flows. *ASME Winter Annual Meeting, New York, Paper* 75-WS/FE-33.

KALLIO, G. A. 1987 Interaction of electrostatic and fluid dynamic fields in wire-plate precipitators. PhD dissertation, Washington State University.

KALLIO, G. A. & STOCK, D. E. 1985 Computation of electrical conditions inside wire-duct electrostatic precipitators using a combined finite-element, finite-difference technique. *J. Appl. Phys.* **59**, 999–1005.

KALLIO, G. A. & STOCK, D. E. 1990 Flow visualization inside a wire plate electrostatic precipitator. *IAS Trans. Indust. Appl.* **26**, 503–514.

KIHM, K. D., MITCHNER, M. & SELF, S. A. 1985 Comparison of wire-plate and plate-plate electrostatic precipitators in turbulent flow. *High Temperature Gasdynamics Laboratory Rep.* J-8. Stanford University.

KUFFEL, E. & ZAENGL, W. S. 1984 *High Voltage Engineering*, pp. 371–377. Pergamon.

KUMARAN, A. R. 1983 Aspects of the fluid mechanics of electrostatic precipitators. *Temperature Gas Dynamics Laboratory Rep.* 15-83-TR. Stanford University.

LARSEN, P. S. & SORENSEN, S. K. 1984 Effect of secondary flows and turbulence on electrostatic precipitator efficiency. *Atmos. Environ.* **18**, 1953–1957.

LAUNDER, B. E. & SPALDING, D. B. 1974 The numerical computation of turbulent flow. *Comput. Meth. Appl. Mech. Engng*, **3**, 259–289.

LEONARD, G. L., MITCHNER, M. & SELF, S. A. 1980 Particle transport in electrostatic precipitators. *Atmos. Environ.* **14**, 1289–1299.

LEONARD, G. L., MITCHNER, M. & SELF, S. A. 1983 An experimental study of the electrohydrodynamic flow in electrostatic precipitators. *J. Fluid Mech.* **127**, 123–140.

MASUDA, S., AKUTSU, K., KANNO, Y. & KO, T. 1979 Motion of small charged particles inside an electrostatic precipitator. In *Proc. IEEE-Industry Application Society Annual Meeting*, pp. 139–145.

MCDONALD, J. R. 1978 A mathematical model of electrostatic precipitation. *US, Environmental Protection Agency Rep.* EPA-500/7-78/111A, Vol. 1.

MELCHER, J. R. 1981 *Continuum Electromechanics*, pp. 3.1–3.2 MIT Press.

PANOFSKY, W. K. H. & PHILLIPS, M. 1952 *Classical Electricity and Magnetism*, 2nd edn, pp. 182–183. Addison–Wesley.

PATANKAR, S. V. 1980 *Numerical Heat Transfer and Fluid Flow*, pp. 105–109. Hemisphere Publishing; McGraw-Hill.

PATANKAR, S. V., BASU, D. K. & ALPAY, S. A. 1977 Prediction of the three-dimensional velocity field of a deflected turbulent jet, *Trans. ASME* I: *J. Fluids Engng* **99**, 758–762.

PATANKAR, S. V. & SPALDING, D. B. 1972 A calculation procedure for heat, mass and momentum transfer in three-dimensional parabolic flows. *Intl. J. Heat Mass Transfer* **15**, 987–1805.

PICKARD, W. F. 1955 Electrical force effects in dielectric liquids. *Prog. Dielectrics*, **5**, 1–39.

RAMADAN, O. E.& SOO, S. L. 1959 Electrohydrodynamic secondary flow. *Phys. Fluids* **12**, 1943–1945.

ROBINSON, M. 1975 Effects of the corona discharge on electric-wind convection and eddy diffusion in an electrostatic precipitator. Ph.D. thesis, The Cooper Union University.

SPIEGEL, M. R. 1975 *Probability and Statistics*, chap. 5. Schaum's Outline Series, McGraw-Hill.

STOCK, D. E. & CROWE, C. T. 1974 The effect of electrohydrodynamic secondary flow in the performance of electrostatic precipitators. In *Proc 1974 Heat Transfer and Fluid Mechanics Institute Meeting*, pp. 254–265. Stanford University Press.

STOCK, D. E. & FADEFF, K. G. 1983 Measuring particle transverse velocity using an LDA. *Trans. ASME* I: *J. Fluids Engng* **105**, 458–460.

THOMSEN, H. P., LARSEN, P. S., CHRISTENSEN, E. M. & CHRISTIANSEN, J. V. 1982 Velocity and turbulence fields in negative corona wire-plate precipitator. *Dept. of Fluid Mechanics Rep.* AFM 82-08. Technical University of Denmark.

VAHL DAVIS, G. DE & MALLINSON, G. D. 1972 False diffusion in numerical fluid dynamics, *University of New South Wales, School of Mech. and Ind. Eng. Rep.* 1972/FMT/1.

WHITE, H. J. 1953 *Industrial Electrostatic Precipitation*, p. 140. Addison-Wesley.

WILLIAMS, J. C. & JACKSON, R. 1952 The motion of solid particles in an electrostatic precipitator. In *Symp. on the Interaction Between Fluids and Particles, Third Congr. of the European Federation of Chemical Engineering*, pp. 282–288.

YABE, A., MORI, Y. & HIJIKATA, K. 1978 EHD study of the corona wind between wire and plate electrodes. *AIAA J.* **15**, 340–345.

YAMAMOTO, T. & SPARKS, L. E. 1985 Effect of turbulent electrohydrodynamics on electrostatic precipitator efficiency. *Gas-Solids Flows, AIAA/ASME 4th Fluid Mechanics, Plasma Dynamics and Lasers Conference. Atlanta, GA.*

YAMAMOTO, T. & VELKOFF, H. R. 1981 Electrohydrodynamics in an electrostatic precipitator. *J. Fluid Mech.* **108**, 1–18.